Gephen R. Sadove

Structurally bound S^{2-}, S^{1-}, S^{4+}, S^{6+} in apatite: The redox evolution of ore fluids at the Philips Mine ore deposit, New York, USA

submitted in partial fulfillment of the requirements for the degree of
Master of Science in Earth and Environmental Sciences
Department of Earth and Environmental Sciences
The University of Michigan

Accepted by:

Signature	Jeffrey Alt Name	4/6/18 Date
Signature	Adam Simon Name	4/9/18 Date
Department Chair Signature	Chris Poulsen Name	4/11/18 Date

I hereby grant the University of Michigan, its heirs and assigns, the non-exclusive right to reproduce and distribute single copies of my thesis, in whole or in part, in any format. I represent and warrant to the University of Michigan that the thesis is an original work, does not infringe or violate any rights of others, and that I make these grants as the sole owner of the rights to my thesis. I understand that I will not receive royalties for any reproduction of this thesis.

☑ Permission granted.

☐ Permission granted to copy after: _____

☐ Permission declined.

Author Signature

Earth and Environmental Sciences
UNIVERSITY OF MICHIGAN

Structurally bound S^{2-}, S^{1-}, S^{4+}, S^{6+} in apatite: The redox evolution of ore fluids at the Phillips Mine ore deposit, New York, USA

Gephen Sadove[1], Brian Konecke[1], Adrian Fiege[2]*, Adam Simon[1]

[1] Department of Earth and Environmental Sciences, University of Michigan, 1100 North University Ave Ann Arbor, MI 48109-1005, USA.
[2] Department of Earth and Planetary Sciences, American Museum of Natural History, Central Park West at 79th Street, New York, NY 10024-5192

**corresponding author*

Abstract

The oxidation state of S plays a critical role in the formation of igneous and magmatic-hydrothermal ore deposits so constraining the oxidation state of S in these systems can be a valuable tool for understanding mineralizing processes. Apatite, commonly $Ca_{10}[PO_4]_6[F,Cl, OH]_2$, is a prevalent accessory mineral in igneous and magmatic-hydrothermal ore-forming systems, and can incorporate redox sensitive elements such as Fe, Mn, and S. Recent experimental studies demonstrate that the behavior of S (e.g., oxidation states of S, S content) in apatite is sensitive to oxygen fugacity. However, there is an overall lack of data with respect to the redox behavior of S in magmatic-hydrothermal systems.

In this study, we used micro X-ray absorption near edge structure (μ-XANES) spectroscopy at the S *K*-edge to measure the oxidation states of S in natural apatite from the Phillips Mine magnetite-sulfide mineral deposit in Putnam County, New York. Here, the data are used to test whether the oxidation state of S in apatite from natural systems

can be used to assess possible fluctuations of oxygen fugacity during primary growth of apatite, and subsequent secondary alteration.

Micro-XANES transects were collected within two apatite grains, starting near the edge of (1) a pyrrhotite inclusion, and (2) an inclusion assemblage consisting of pyrite, ferroan carbonate, pyroxene, and magnetite. Transects were conducted moving away from the inclusions and into the apatite host. Electron probe micro-analysis (EPMA) transects were performed parallel to the μ-XANES transects to correlate changes in the oxidation state of S in apatite with changes in the S concentration of apatite. The XANES analyses reveal that apatite contains variable proportions of S^{6+}, S^{4+}, S^{1-} and S^{2-}, with corresponding peak absorption energies of 2481.8 ± 0.3 eV, 2477.9 ± 0.4 eV, 2471.8 ± 0.1 eV, and 2469.8 ± 0.04 eV, respectively. Peak areas determined for the different oxidation states of S in apatite demonstrate systematic variations in $S^{6+}/\sum S$, where elevated $S^{6+}/\sum S$ ratios typically coincide with higher concentrations of S and rare earth elements (REEs) in apatite. The observation of multiple oxidation states of S, and the presence of monazite inclusions that record secondary, fluid-mediated dissolution-reprecipitation of apatite, indicate differences in S and oxygen fugacity during primary mineralization and secondary metasomatism. We propose that the apatite grains crystallized from hydrothermal conditions where reduced S, i.e., sulfide (or H_2S in the fluid; HS^-; S^{2-}), was the dominant stable S species. Subsequently, metasomatism of apatite in the presence of an oxidized fluid; e.g., elevated SO_2/H_2S, resulted in the exsolution and growth of monazite, and the incorporation of oxidized S (S^{6+} and S^{4+}) in apatite. This study demonstrates that the oxidation states of S in apatite can provide

valuable geochemical information regarding the redox evolution of magmatic-hydrothermal systems.

Keywords: Apatite; Sulfur oxidation states; Sulfur micro-XANES; Oxygen fugacity; Rare earth elements; Hydrothermal ore deposits

1. Introduction

Sulfur is a polyvalent element (S^{2-}, S^{6+}, S^{4+}, S^{1-} and S^{2}) that occurs in terrestrial, and extraterrestrial geological systems (Carroll and Rutherford, 1988; Nilsson and Peach, 1993; Wallace and Carmichael, 1994; Carroll and Webster, 1994; Nagashima and Katsura 1973; Katsura and Nagashima, 1974; Paris et al. 2001; Jugo et al. 2010). The oxidation state of S is the key variable that controls the solubility of S in silicate melts and hydrothermal fluids, and the partitioning of S between minerals, melts, and fluids (e.g., Keppler, 1999; Jugo et al. 2009; Simon and Ripley, 2011; Zajacz et al. 2012; Fiege et al. 2015). In magmatic and hydrothermal environments, S plays a critical role in the formation of several different ore deposit types, including porphyry, iron oxide - copper - gold, volcanogenic massive sulfide, and magmatic sulfide deposits (Wood et al. 1987; Barnes and Lightfoot, 2005; Mungall et al. 2005; Williams-Jones and Heinrich, 2005; Simon and Ripley, 2011). The oxidation state of S imparts a major control on the mobility, transport and enrichment of metals (e.g., Au, PGE's), that ultimately give rise to economic mineral deposits (Simon and Ripley, 2011). For example, reduced S (i.e., S^{2-}, S_3^-) efficiently complexes with, and transports gold in aqueous fluid, whereas oxidized S (i.e., S^{4+}, S^{6+}) is an inefficient complexing ligand for gold (Zajacz et al. 2012; Pokrovski and Dubrovinsky, 2011; Pokrovski and Dubessy, 2015; Fontboté et al. 2017). These redox dependent systems, and characteristics of S, triggered many studies to identify ways to determine S activity, and explain

the effect of oxidation state on the ore forming potential in geologic systems (e.g., Toulmin and Barton, 1964; Crerar et al. 1978; Wood and Samson, 1998; Mengason et al. 2010).

One method to investigate terrestrial and extraterrestrial geologic systems is by analyzing apatite - [$Ca_{10}(PO_4)_6(F,Cl,OH)_2$]. Apatite is the focus of numerous studies owing to its ability to structurally incorporate S and record S activity in magmatic and hydrothermal systems (e.g., Streck and Dilles, 1998; Parat et al. 2002, 2011; Piccoli and Candela, 2002; Hughes and Rakovan, 2002). Apatite can incorporate S as a trace element, preferably in the sulfate state, when replacing PO_4^{3-} in the minerals structure (Parat et al. 2011; Konecke et al., 2017a; Kim et al., 2017). Investigating the oxidation state of sulfur in apatite, in combination with volatile and trace element contents (here mainly F, Cl, Ce, S), yields unique information about the behavior of S and the processes that drive its enrichment or depletion. Previous findings show that apatite is capable of incorporating higher concentrations of S under relatively oxidizing conditions, e.g., where reduced S is the dominant oxidation state of S in the system (e.g., Rouse and Dunn, 1982; Liu and Comodi, 1993; Tepper and Kuehner, 1999; Parat et al. 2011; Konecke et al. 2017a). This led to the hypothesis that the concentration of S in apatite could be used to deduce changes in oxidation state during the evolution of a particular system (e.g., Lyons, 1988; Peng et al. 1997; Piccoli and Candela, 2002; Parat et al. 2004, 2011; Webster and Piccoli, 2015; Mao et al. 2016). Streck and Dilles (1998) report that the concentration of S in apatite from the Yerington batholith, Nevada, decreases from ~0.4 S wt % in the core to <0.08 S wt% in the rim. The systematic decrease of S during growth of apatite, was interpreted as a temporal record of the evolution of the magma wherein crystallization of anhydrite causes a decrease in the concentration of S in the silicate melt, which is reflected in the core-to-rim zonation of S in apatite. Streck and Dilles (1998) and other studies (e.g., Parat et al. 2011) were not able to state definitively that the S in apatite was oxidized

S, but suggested sulfate as the only relevant S species in apatite. Those authors, and other studies, relied on compositional variations to assess the incorporation mechanisms of S and other trace elements into the apatite structure:

$S^{6+} + Si^{4+} \leftrightarrow 2P^{5+}$ (Parat et al. 2011)

$REE^{3+} + Si^{4+} \leftrightarrow Ca^{2+} + P^{5+}$ (Parat et al. 2011)

$S^{6+} + Na^{+} \leftrightarrow P^{5+} + Ca^{2+}$ (Parat et al. 2011)

$S^{6+} + S^{4+} \leftrightarrow 2P^{5+}$ (Konecke et al. 2017a)

$2PO_4^{2-} \leftrightarrow SO_4^{2-} + SO_3^{2-}$ (Kim et al. 2017)

Recently, Konecke et al. (2017a) demonstrated that there is a systematic relationship between the integrated peak area ratios of each oxidation state of S in apatite (e.g., $S^{6+}/(S^{6+} + S^{4+} + S^{2-} + S^{1-})$; hereafter reported as $S^{6+}/\sum S$), and the oxidation state of the magmatic system. Those authors used X-ray absorption near-edge structure (XANES) spectroscopy at the S K-edge to measure in situ the oxidation states of S in apatite grains that were grown experimentally at different oxygen fugacities (f_{O2}). Konecke et al. (2017a; 2017b) report sulfate and sulfite as the only oxidation states of S in apatite in oxidizing to intermediate environments ((f_{O2}) = FMQ +1.2 and +3; FMQ = fayalite-magnetite-quartz solid buffer), whereas sulfide dominates over sulfate at reduced conditions of ≤FMQ. Ab-initio quantum mechanical calculations by Kim et al. (2017) confirm that apatite can incorporate S^{2-}, S^{4+} and S^{6+} via several possible coupled substitutions. The results of Konecke et al. (2017a; 2017b) and Kim et al. (2017) offer the potential to measure, and use, the oxidation state of S in apatite to examine the evolution of redox conditions of natural systems.

In this study, we used XANES to assess directly the oxidation states of S in apatite grains from the Phillips Mine magnetite-sulfide mineral deposit in Putnam County, New York, U.S.A. The XANES data are combined with electron probe micro-analysis (EPMA), cathodoluminescence (CL) imaging, back-scattered electron (BSE) imaging, and wavelength dispersive spectroscopy (WDS) element mapping to examine the chemistry of the apatite grains and the hydrothermal system from which the apatite crystallized. The results reveal changes in the oxidation state of S in apatite that fingerprint the original reducing (i.e., S^{2-}, S^{1-}) conditions during mineralization, and oxidizing (i.e., S^{4+}, S^{6+}) conditions during post-mineralization hydrothermal alteration.

2. Geologic background

The Phillips Mine-Camp Smith area is located in the Hudson Highlands, and serves as an example for several iron deposits located in southeastern New York. The mines overlay the Grenville basement spanning New York, New Jersey, Pennsylvania and Connecticut (Fig. 1; Kalczynski and Gates, 2014). Specifically, the Phillips Mine is located on the North flank of Anthony's Nose peak, at the east end of Bear Mountain Bridge, North of Peekskill, NY, and east of the Hudson River (41.3256° N, 73.9514° W; Fig. 1; Klemic et al. 1959; Groves et al. 2010).

Mining activity dates to the early nineteenth century when the deposit was exploited for iron ore (Robinson, 1825; Beck, 1842; Betts, 1997). Iron mining was short lived, owing to the relatively high abundance of sulfides and apatite that decrease the ore grade. The deposit was mined for copper starting in the 1860s, and is identified in 1872 as the Hudson River Copper Mine. In the 1880s, the mine produced sulfides for production of sulfuric acid (Kemp, 1894). Efforts were made to reopen the mine for Cu in the early twentieth century, but it was the discovery of uraninite that stimulated significant interest in the 1950s. However, later drilling indicated that the

U concentrations were not economic and no further mining activity was pursued (Klemic et al. 1959).

The mine is part of a northeastward-trending belt of Precambrian crystalline rocks that are bound by faults on the southeast and northwest. Sulfides and oxides are disseminated in host rocks that include diorite, granite, mafic dikes, metamorphosed Precambrian sedimentary rocks, hornblende pegmatite, and gneiss. The main ore body at the Phillips Mine is lenticular in shape, approximately 30 m wide and > 90 m deep, and hosted in hornblende pegmatite. The ore body dips to the northwest at about 70 degrees and strikes northeast following the direction of surrounding formations. The ore body is comprised of both disseminated and massive mineralization, e.g., mainly massive pyrrhotite (with as much as 3 wt% Ni), along with pyrite, magnetite and chalcopyrite (Loveman, 1911; Klemic et al. 1959). The thickness of the ore body thins to the southwest, and remains unexposed to the northeast. The ore is S-rich, containing as much as 30 wt% S, up to 0.5 wt% Cu, and 0.3 - 3 wt% Ni (Kemp, 1894; Klemic et al. 1959).

Klemic et al. (1959) report the following paragenetic sequence from oldest to youngest: uraninite, magnetite, pyrite, chalcopyrite, and pyrrhotite. A maximum age of 920 Ma for mineralization was determined by U-Pb dating of uraninite (Klemic et al. 1959). Textural relations indicate that pyrrhotite precipitated in open space, and also replaced hornblende. Gangue minerals include feldspar, pyroxene, hornblende, epidote, calcite, augite, pyroxene, quartz, and apatite (Zodac, 1933).

3. Sample description

Hand samples were collected in the open mine dumps leading up to the main mine shaft. Apatite grains, translucent to opaque brown in color, contain inclusions of pyrrhotite (Po), pyrite (Py),

magnetite (Mt), ferroan carbonate (Cb), pyroxene (Pyx) and monazite (Mnz). The two grains, referred to in this study as grain A and grain B, were chosen for detailed analyses as described below.

4. Methods

4.1. Electron probe micro-analysis (EPMA)

The two apatite grains from the Phillips Mine were first mounted in epoxy and polished for observation by using a petrographic microscope and back-scattered electron (BSE) imaging. Quantitative characterization of the apatite grains was made by using a CAMECA SX–100 electron probe micro-analyzer (EPMA). Analyses were conducted at the Electron Microbeam Analysis Laboratory (EMAL), University of Michigan (UM, Ann Arbor, USA), and at the American Museum of Natural History (AMNH, New York, USA).

Electron probe micro-analyzer was used to measure the major, and trace element compositions (i.e., P, Ni, Cl, F, Ca, Na, K, Mg, Ti, Mn, S, Sr, Ba, Al, Si). The samples were carbon coated and peak counting times of 20 s were used for all elements, except 5 s for F, and 50 s for Ni. An acceleration voltage of 15 kV, a beam current of 10 nA, and a beam size of 2 μm were used for all elements, except for S (Table 1; Supplemental Data Table S1-S4). Fluorine measurements were monitored for evidence of beam-induced migration (Goldoff et al. 2012). A second beam condition of 15 kV, 35 nA, 1 μm beam, and counting times of 60 - 300 s was used to analyze S. Two different EPMA sessions to categorize the S in apatite resulted in detection limits of 30 μg/g and 58 μg/g S (Supplemental Data Table S4). Consistent with Konecke et al. (2017a), this procedure produced reliable results, confirmed by frequent monitoring of Durango apatite as a secondary check standard (e.g., F contents are reproduced within 1 sigma uncertainty of ± 0.3 wt%). For EPMA line transects 1 and 6-9 we measured the S content in trace mode, using the

previously determined average composition of the Phillips Mine apatite for matrix correction (Supplemental Data Table S4). The OH content of apatite for each individual EPMA spot can be estimated with the constraint that the halogen site is filled by $X_F + X_{Cl} + X_{OH} = 1$ (Hughes and Rakovan, 2015). We used the method of Ketcham et al. (2015) to calculate the OH concentration in apatite (Supplementary Data Tables S1 and S4).

Concentrations of S, Fe, Ni, and O in pyrrhotite, pyrite, and magnetite were analyzed by using an acceleration voltage of 20 kV, a beam current of 50 nA, and a focused beam (Supplemental Data Table S2). Major and trace elements (i.e., Mg, Al, Si, Ti, Ca, P, V, Cr, Fe, Mn) in pyroxene were analyzed by using an acceleration voltage of 20 kV, a beam current of 30 nA, and a focused beam (Supplemental Data Table S3). Prior to analysis of Mg, Ca, Mn, Fe, and C concentrations in the ferroan carbonate phase, the samples were re-polished extensively, ultrasonicated, and gold-coated. The ferroan carbonate phase was analyzed at an acceleration voltage of 15 kV, a beam current of 10 nA, and a beam size of 10 μm (Supplemental Data Table S3).

4.2. Cathodoluminescence (CL) imaging and Wavelength Dispersive Spectroscopy (WDS) mapping

A JEOL JSM - 7800 FLV field emission scanning electron microscope (FE-SEM), fitted with a Gatan ChromaCL2 CL imaging detector, was used to further characterize the apatite grains. The FE-SEM was used to generate high-resolution CL images and energy dispersive spectroscopy (EDS) elemental maps of the apatite grains. An accelerating voltage of 15 kV was used for the CL imaging and 15-20 kV for the EDS element mapping. Additionally, EDS point analyses on the FE-SEM were used to identify monazite present in the apatite grains (maps not shown).

The electron probe was also used to generate qualitative element compositional maps for S, Na, Cl, and Ce by using wavelength dispersive spectroscopy (WDS) with an acceleration voltage of 15 kV, beam current of 100 nA, dwell time 0.1 s, and a focused beam

4.3. Sulfur X-ray absorption near edge structure spectroscopy (S XANES)

Micro-XANES spectroscopy line scans were collected on the Phillips Mine apatite grains A and B. The measurements were conducted at the Advanced Photon Source (APS), GSECARS 13-ID-E beamline, Argonne National Laboratory (USA). The beamline uses a high-flux beam ($\geq 4.5 \times 10^{10}$ photons/s/100 mA/mm^2) that, by using Kirkpatrick-Baez (KB) focusing mirrors, can generate a spatial resolution micro-focused spot size beam of 2 x 1 μm, with an energy range of 2.4-28 kV. The XANES spectra were collected at an energy range of 2450-2540 eV, with step size of 0.1- 0.3 eV at the S K-edge (2464-2482 eV). Two scans per step, with step scan durations of 1-3 scans per energy step, were used to reach higher S X-ray counts needed for spectra of high-quality and to analyze S in the apatite grains.

There is a shift in energy (~12 eV) of the S *K*-edge between S^{2-} and S^{6+}. This difference allows the assessment of the valence of S in unknown samples by measuring the shift in energy of the absorption edge (Paris et al. 2001). We compared our spectra from unknown samples with spectra for known S species of particular oxidation state. Reference material included Durango apatite (sulfite, S^{4+}, peak near 2478 eV and sulfate, S^{6+}, ~2482 eV), sodium sulfite (S^{4+}, ~2478 eV), pyrite (S^{1-}, ~2471eV), pyrrhotite (sulfide, S^{2-}, characterized by having both a sharp peak at ~2470 eV and a broad peak at ~2476 eV), and double-sided adhesive tape (sulfate, S^{6+}, all session value: 2481.8 ± 0.06 eV, 1σ error; see Fig. 2; Fig. S1; Fleet, 2005; Konecke et al. 2017a)

We emphasize that prolonged exposure of apatite to the high-flux photon beam at the 13-ID-E beamline does not affect the oxidation state of S in apatite as shown by Konecke et al.

(2017a). However, the samples were re-polished extensively, prior to each XANES session, to prevent possible electron beam irradiation damage generated during EPMA that could affect the oxidation state of S in apatite.

Four XANES line transects (red dotted arrows; Fig. 3; Fig. 4) were collected on the two apatite grains starting near the edge of: (1) a pyrrhotite inclusion (transect lengths = 60 - 70 μm; grain A), and (2) an inclusion assemblage consisting of pyrite, ferroan carbonate, pyroxene, and magnetite (transect lengths = 90 - 120 μm; grain B), moving away from the inclusions and into the apatite host (Fig. 3E, 4E). The apatite-inclusion interface is inferred with 2-3 μm uncertainty, considering the precision of the stage and the spot size.

4.3.1. Data Processing - Peak area integration & spectra correction of S XANES spectra

The software package Athena (Ifeffit package, Ravel and Newville, 2005) was used to normalize the pre- and post-edge, and merge the raw XANES spectra. The curve and peak fitting software, Fityk, (Wojdyr, 2010) was used for peak area integration. For background fitting, an exponentially modified Gaussian (EMG) function, with a set inflection position at 2478-2480 eV, was used. The Gaussian A (i.e., area) function was then applied to fit the ionization peak (if present) and energies for S^{6+}, S^{4+}, and S^{2-} (including both broad and sharp peaks). The peak area ratios of the oxidation states of S were used to test and demonstrate changes in the oxidation state of S in apatite. The spectra that contained S^{6+} were used, and integrated as $S^{6+}/\sum S$ peak area ratios [$S^{6+}/\sum S_{area}$; e.g., $\sum S_{Total} = (S^{6+} + S^{4+} + S^{1-} + S^{2-})$] to correlate with μg/g S. Durango apatite was used as a check standard for XANES analyses. The intra-session average integrated $S^{6+}/\sum S_{Total}$ peak area ratio for Durango apatite = 0.954 ± 0.003 eV (1σ standard error) is consistent with values reported by Konecke et al. (2017a).

5. Results

5.1. Sample Characterization using BSE imaging, CL, EDS, and WDS element mapping

Inclusions of pyrrhotite (Po; length of ~0.8 mm), pyrite (Py; <60 μm), magnetite (Mt; ~110 μm), monazite (Mnz; <10 μm), pyroxene (Pyx; <35 μm), and Fe-carbonate (~260 μm) were identified in the apatite through a combination of BSE imaging, EDS point analyses and WDS element mapping (Fig. 3; Fig.4). Monazite is observed in veins cutting through the apatite grains as well as distributed throughout as inclusions (Fig. 3C). Energy dispersive spectroscopy identified rare earth element-rich inclusion (i.e., monazite) within apatite, and O-Fe-Ni-S altered assemblage within the pyrrhotite. Cathodoluminescence (CL) images of apatite illustrate blue-violet dominant color luminescence with complex zoning (Fig. 3D, 4D).

In Figure 5, semi-qualitative WDS maps of S, Cl, and Ce are compared with a CL image for the same portion of an apatite grain. Higher counts for Ce, Cl, and S (Fig. 5C-E) often correlate with light colored zones in the CL image (Fig. 5B). Lighter zones in CL also show higher S μg/g while darker colored zones, in CL, indicate lower S μg/g. For example, in Fig. 6 transect 1, low S concentration (position 29-45 μm; Fig. 6A, Fig.7) correlates with darker CL zones (Fig. 3E), whereas, more CL active (brighter) zones correlate with higher S concentrations (between 50-80 μm).

Generally, S, Cl, and Ce counts correlate spatially within the apatite grain, aside from in the veinlet running across the apatite grain (Fig. 5E), that is S-bearing only. Also, different degrees of S enrichment are observed in regions which are otherwise evenly enriched in Cl. Cerium shows localized enrichment (highest counts/ “bright-globules”) in veins which are attributed to the presence of monazite. Similarly, localized S “bright-globules” (length <10 μm) are observed near

cracks and in veins. The EDS elemental maps do not indicate overlap with other elements (i.e., Fe, Ni, Cu, Ca), hence the S-rich globules may represent native S inclusions.

5.2. EPMA and XANES

The Phillips Mine apatite grains are characterized as fluorapatite, containing on average 2.4 wt% F, 0.5 wt% Cl and 0.86% OH* wt% (*calculated based on stoichiometry; see Table 1 and Fig. 8; Fig. S2; Hughes and Rakovan, 2015; Ketcham, 2015). The S concentration in the apatite grains is highly variable (Fig. 6 and 7); e.g., average S content in the grains is approximately 190 μg/g, and varies from <100 μg/g S to ~930 μg/g S (Fig. 9A). Higher concentrations of S typically correlate spatially with increased REE contents, up to 5,000 μg/g ($Ce_2O_3 \pm La_2O_3$; hereafter REE_{tot}; Fig. 6E is representative of the nine EPMA transects), which are consistent with the WDS maps and CL images (Fig. 5).

Similar to S concentration fluctuations throughout the apatite, S also ranges within the pyrrhotite inclusion. The EPMA point analyses of the O-Fe-Ni-S altered zones within the pyrrhotite inclusion show increased S contents (51-42 wt% S), lower Fe content (50-33 wt% Fe), and higher Ni (~1 wt%) when compared to the pyrrhotite itself (~39 wt% S; ~59 wt% Fe; 0.5 wt% Ni; Supplemental Data Table S2 and Fig. S3). Additional point analyses were conducted on other unknown phases, and reveal carbonate incorporating 41.6-51.2 wt% Fe (hereafter considered as ferroan carbonate; Supplemental Data Table S3; Fig. 4C).

Aside from point analyses, nine EPMA line transects were collected (transect lengths = 75 - 104 μm) away from pyrrhotite (in grain A) and pyrite-containing (grain B) inclusions. Most transects were parallel and proximal to the four XANES transects in order to correlate changes in oxidation state of S with concentration of S, and other elements, in apatite (see Fig. 3 and 4). Analyses of apatite adjacent to sulfide grains could yield spuriously high S contents due to the

secondary fluorescence of the sulfide grains (cf. Llovet and Galan, 2003; Fig. S4). Modeling of the secondary fluorescence effects using the PENEPMA software (Llovet and Salvat, 2016) show that secondary fluorescence would contribute <1 μg/g S measured in apatite for points greater than 50 μm from an apatite-sulfide boundary. Specifically, at approximately 30 μm from the interface, measured concentrations will be artificially higher by 10 μg/g, at approximately 12 μm from the interface, measured concentrations will be 100 μg/g higher (e.g., Fig. 7B), etc. Thus, few analyses (e.g., first spots in transects 1, 4, and 7) are notably affected by secondary fluorescence. While these particular results need to be interpreted with caution, we highlight that the effects are typically negligible, and do not change the interpretation of this study. Furthermore, modeling of the volume of material intersected by the electron beam using CASINO Monte-Carlo simulation software (Drouin et al. 2007) indicates that S Kα X-rays are generated within approximately 1.2 μm of the sample surface. Since the penetration depth of soft X-rays at the S *K*-edge by use of XANES is approximately 0.2 μm (Troger et al. 1992; Fleet, 2005), analytical artifacts or fluorescence of sulfides is unlikely.

The XANES transects show that the apatite grains consist of variable ratios of S oxidation states: sulfate (S^{6+}; 2481.8 ± 0.3 eV), sulfite (S^{4+}; 2477.9 ± 0.4 eV), monosulfide (S^{1-}; 2471.8 ± 0.1 eV), and disulfide (S^{2-}; 2469.8 ± 0.04 eV; 1σ error; Fig. S1). Location of the XANES transects within the apatite is confirmed by comparing the intensity of normalized and unnormalized spectra (Fig. S5). The low intensity of the S in apatite unnormalized spectra indicates the location of the collected spectra within the apatite while the high intensity indicates location within the iron sulfide.

Sulfur peak areas ($S^{6+}/\sum S_{area}$) demonstrate systematic variations in $S^{6+}/\sum S_{area}$ (on average 0.30 ± 0.4 eV, 1σ error; Fig. 9B), where elevated $S^{6+}/\sum S_{area}$ ratios typically coincide with higher

concentrations of S and rare earth elements (Fig. 10). We highlight that the provided $S^{6+}/\sum S_{area}$ values are "integrated peak area ratios" that are used to evaluate relative changes in the oxidation states of S, and not explicitly absolute concentration ratios. However, due to the fitting method developed by Konecke et al. (2017a) involving precise background fitting, the integration of each absorption peak may yield near-quantitative results.

Table 1. Apatite A and B - EPMA Analyses
wt% oxide

Sample	Apatite A: AA2-3	Apatite B: AB1-7	SD wt% oxide	Det limit (µg/g)
F	2.43	2.23	0.26	2344
Cl	0.55	0.53	0.04	188
Na_2O	b.d.	b.d.	0.04	440
K_2O	b.d.	b.d.	b.d.	279
MgO	b.d.	0.02	0.01	236
CaO	55.01	0.67	1.71	366
SiO_2	0.25	42.08	0.08	1311
P_2O_5*	41.79	54.13	0.67	713
TiO2	b.d.	b.d.	0.01	488
MnO	b.d.	b.d.	0.04	282
FeO	b.d.	0.02	0.06	69
SrO	b.d.	b.d.	0.06	740
BaO	b.d.	b.d.	0.10	716
Al_2O_3	b.d.	b.d.	0.02	1588
La_2O_3	b.d.	b.d.	b.d.	1812
Ce_2O_3	0.15	b.d.	0.09	1809
SO_2	0.01	b.d.	0.01	894
O = (F,Cl)	1.15	1.06		
OH wt% calc.	99.87	99.66		
Total	0.82	1.03		
S (µg/g)	57.6	87.6		
F**	1.34	1.22		
Cl**	0.16	0.16		
OH**	0.49	0.62		
F +Cl + OH	2.00	2.00		

Notes:
2 selected samples from each apatite grain are presented.
b.d. is bellow detection limit.
Calculated as OH assuming the halogen site is filled with F + Cl + OH.
O=F,Cl is correction factor.
SD wt% oxide averages are presented for each oxide.
Average SD for F and Cl represented in wt%.
Analyses given in 1σ standard error of mean.
* P_2O_5 drift was detected and corrected based on systematic shift in both unknown and durango apatite measurment.
** Data used in ternary plot.

6. Discussion

6.1. Chemical and mineralogical evidence for metasomatic alteration

Apatite can record metasomatic reactions that result in mass transfer of elements such as S and REEs between the fluid and the apatite, altering the original chemical composition of apatite (Harlov, 2015). Chemical alteration is not limited to diffusive exchange mechanisms, but includes dissolution-reprecipitation reactions (Harlov, 2015 and references therein). The presence of (secondary) monazite in the Phillips Mine fluorapatite grains (Fig. 3, 4) suggests secondary growth, during hydrothermal alteration, due to coupled dissolution–precipitation reaction; where the hydrothermal fluid migrates through interconnected, three dimensional nano- and micro-porosity structures, the apatite becomes depleted in REEs ± Na + Si (Harlov and Förster, 2003; Harlov, 2015; Betkowski et al. 2016). The REEs initially dissolved within the apatite structure are exsolved during reactions with the fluid, and manifest as [REE]PO_4 mineral inclusions. The exsolution process of [REE]PO_4 includes Na and Si that are preferentially removed from apatite by the fluid, which by mass balance increases the concentrations of REE at the apatite-fluid interface, and culminates in local [REE]PO_4 supersaturation and nucleation (Wolf and London, 1995). The result is an apatite domain that is enriched in LREEs, and another domain that is depleted in these elements and contains, or is proximal to, monazite inclusions (Harlov et al. 2002).

The fluorapatite also hosts an inclusion of pyrrhotite. The pyrrhotite exhibits S-Ni-rich and Fe-poor (relative to end-member pyrrhotite) dendritic-like domains that are consistent with alteration (Fig. 3C). These changes in concentration possibly formed as a result of metasomatism, which caused oxidation of pyrrhotite, and remobilization of the S-Fe-Ni (Supplemental Data Table S2 and Fig. S3A). The WDS element maps (Fig. 5E) show higher counts in the S-bearing veinlet

only, compared to the Cl and Ce maps, which further supports the involvement of a S-bearing fluid in the apatite.

Other evidence for fluid-mediated metasomatism of the apatite grains is shown in CL images, which exhibit strong variations in violet luminescence. Cathodoluminescence in apatite is not produced by halogens, but rather is the result of trace element substitutions into the apatite structure (Waychunas, 2002). The intensity and perceived color of luminescence are due to the presence of specific ions, or groups of ions, most commonly Mn^{2+}, which causes yellow luminescence, and REE^{3+} that cause violet-blue luminescence (Götze et al. 2001; Waychunas, 2002; Kempe and Götze, 2002; Götze, 2012). Variations in the concentrations of Mn^{2+} and REE^{3+} at the (μg/g) level can cause observable changes in the CL intensity as well (Gros et al. 2016). The apatite grains from the Phillips Mine show blue-violet CL emission similar to other hydrothermal iron ore deposits, such as the Cerro de Mercado mine in Durango, Mexico, in the Grenville formation at Mineville, New York, and in the Atlas Mountains of Morocco (Waychunas, 2002). As with the Phillips Mine, these deposits contain fluorapatite that displays blue-violet emission, and is dominated by Ce^{3+} activation (Waychunas, 2002).

The CL zonation in the apatite grains is coincident with variations in the abundances of REE and S (Fig. 5 and 7E). These variations suggest remobilization of Ce, due to a S bearing fluid event, that later reprecipitated and formed monazite and the REE-rich vein (Fig. 3C). The CL image in Fig. 5B shows patchy zoning, interpreted as affiliated with this fluid event. Another independent fluid event may have occurred, as the WDS relative intensity maps of Cl, Ce, and S (Fig. 5) do not correlate in the veinlet (Fig. 5E), which is high only in S. A separate fluid event may have resulted in the overall spatial correlation between the three elements (Cl, S, Ce). Lastly,

the native S globules (e.g., $S_{7\text{-}8;}$ Fig. 5E) perhaps formed during cooling of trapped fluid inclusions in the apatite, as proposed in previous studies of similar systems (Beny, 1982; Barré et al. 2015).

6.2. Sulfur oxidation states in hydrothermal apatite: Implications for ore forming processes

The S XANES measurements demonstrate the presence of four oxidation states of S in the Phillips Mine apatite grains: S^{2-}, S^{1-}, S^{4+}, and S^{6+} which reflect a range of f_{O2} environments (Fig. 2). The apatite grains are typically low in S (often <200 μg/g S) and these S-poor areas are dominated by reduced S species ($S^{6+}/\sum S_{area} < 0.4$; often < 0.2; Fig. 9; Fig. 10). Conversely, S-rich areas (up to 930 μg/g S) are characterized by $S^{6+}/\sum S_{area}$ values that approach 1.0. The chemical, textural, and the ratio correlations described above indicate a formation of the apatite by a reduced fluid, probably in the presence of sulfides. Subsequently, an oxidized fluid altered the apatite resulting in the formation of sulfate-rich apatite regions through dissolution-reprecipitation reactions. Here, it remains unclear if this fluid was rich in oxidized S or if the fluid simply had an oxidizing character, which resulted in the dissolution of sulfide and the oxidation of sulfide to sulfate.

The S^{1-} regions observed in the apatite mark the first report of this oxidation state in the literature, and may have formed as a result of hydrothermal alteration near the pyrite. Here, the pyrite and apatite are either (1) locally dissolved and S^{1-} is incorporated into apatite during re-precipitation, or (2) S^{1-} is introduced through diffusive exchange in solid state. The latter scenario only requires a heat source and is favored because during dissolution-reprecipitation reactions S^{1-} may not be the stable species in the fluid phase. However, the presence of significant amounts of S_3^- radicals in the fluid (e.g., Pokrovski and Dubrovinsky, 2011; Pokrovski and Dubessy, 2015;

Fontboté et al. 2017) may allow the transfer of S^{1-} from the pyrite to the apatite by solid state diffusive exchange (2).

6.3. A model for the formation of the Phillips Mine apatite

The magnetite-pyrite-pyrrhotite assemblage is common in hydrothermal sulfide-oxide mineral deposits (Barnes and Czamanske, 1967; Hall, 1986), where mineralization is driven by changes in temperature, pH of the ore fluid, and redox conditions (Fontboté et al. 2017). The following equilibria, from Crerar et al. (1978), describe how changes in pH and redox conditions can cause precipitation of pyrrhotite, pyrite, and magnetite from a hypogene ore fluid:

Pyrite:

$$FeS_2 + 2H^+ + nCl^- + H_2O_{(l)} = 2H_2S_{(aq)} + FeCl_n^{2-n} + \frac{1}{2}O_{2(g)} \qquad (1)$$

Magnetite:

$$Fe_3O_4 + 6H^+ + 3nCl^- = 3H_2O_{(l)} + 3FeC1_n^{2-n} + \frac{1}{2}O_{2(g)} \qquad (2)$$

Pyrrhotite:

$$FeS + 2H^+ + nCl^- = H_2S_{(aq)} + FeCl_n^{2-n} \qquad (3)$$

The observations in the present study are most plausibly consistent with two distinct hydrothermal events, illustrated schematically in Fig. 11. The first stage involves precipitation of pyrrhotite, pyrite, magnetite, and apatite from a reduced ore fluid (Fig. 11A-B), while the second stage involves post-mineralization coupled dissolution-reprecipitation of apatite in the presence of an oxidized hydrothermal fluid (Fig. 11C-F). Experimental data demonstrate that the solubilities of Fe and S in a reduced hydrothermal fluid decrease with decreasing temperature (Crerar et al, 1978). In the case of the Phillips Mine, Klemic et al. (1959) describe replacement textures where sulfides and oxides replaced silicate phases such as feldspar, hornblende and augite. The paragenetic sequence reported by Klemic et al. (1959) in order of mineral precipitation is

magnetite, pyrite, chalcopyrite, pyrrhotite. Small fluctuations in redox conditions during cooling and water-rock interaction can drive the ore fluid into the pyrrhotite stability field, consistent with pyrrhotite being the most modally abundant sulfide in the Phillips Mine ore body. Further, water-rock reactions between the ore fluid and the host rocks cause the pH of the ore fluid to increase, owing to loss of hydrogen during hydrolysis of feldspar to sericite, as described by the Crerar et al. (1978) reaction:

$$3KA1Si_3O_8 + 2H^+ = KA1_2\ A1Si_3O_{10}(OH)i + 2K^+ + 6SiO_2 \qquad (4)$$

(orthoclase) (sericite)

Klemic et al. (1959) report that feldspar, in the host rocks, is ubiquitously altered to sericite. Increasing the pH of the ore fluid by one log unit, as it percolates through the host rock, decreases the solubility of Fe in the ore fluid by two orders of magnitude (Crerar et al. 1978). Oxidation of the ore fluid and increasing pH also decrease the solubility of S in the ore fluid and trigger precipitation of metal sulfides. Thus, the combination of decreasing temperature and increasing pH of the ore fluid are the most plausible explanations for the precipitation of sulfides and oxides that formed the primary mineral assemblage at the Phillips Mine.

Apatite is a common mineral in hydrothermal ore deposits, and it is plausible that apatite co-crystallized with the primary assemblage pyrrhotite - pyrite - magnetite. Primary apatite precipitating from a reduced hydrothermal S-bearing fluid will incorporate reduced S, as S^{2-} and S^{1-}, as revealed by the S XANES analyses reported in this study. A second hydrothermal event is interpreted by the presence of exsolved monazite in apatite and the strong zonation of REEs, Cl, and S within the apatite grains (Fig. 3 and 4). The S XANES analyses show that domains within the Phillips Mine apatite are enriched in oxidized S (mainly S^{6+}), an observation that is consistent with metasomatism caused by an oxidized hydrothermal fluid. Lastly, the ferroan carbonate,

encapsulating magnetite, pyroxene and pyrite (Fig. 4C), may be primary or an alteration phase (of sulfides) by an oxidized CO_2-bearing fluid that is a common constituent in skarn deposits (Meinert, 1992).

7. Conclusions

Sulfur XANES data reveal that the apatite grains from the Phillips Mine hydrothermal sulfide-magnetite mineral deposit contain structurally bound S^{2-}, S^{1-}, S^{4+}, S^{6+}. This study is the first to report four different oxidation states of S in natural apatite. Varying proportions of these structurally bound oxidation states were observed throughout the grains. Here, the $S^{6+}/\sum S_{area}$ ratio ranges from zero sulfate to sulfate-only and the abundance of S in apatite correlates positively with the abundance of oxidized S (S^{4+} and S^{6+}). Interpretations are consistent with the ability of apatite to incorporate higher concentrations of oxidized S relative to reduced S in magmatic systems (Parat et al. 2011; Konecke et al. 2017a). The presence of monazite fingerprints fluid-mediated dissolution-precipitation of originally REE-bearing apatite. This finding, of multiple oxidation states of S, and the presence of monazite inclusions that record secondary dissolution-reprecipitation of apatite, indicate differences in S and oxygen fugacity during primary mineralization and metasomatism. This study demonstrates that the transition from S^{2-} to S^{6+} may occur over a narrow interval, and that the oxidation state of S in apatite provides valuable geochemical information regarding the redox evolution of magmatic-hydrothermal systems. The study shows that S can no longer be reported solely as sulfate species, and care should be taken to identify the specific oxidation state. Lastly, previous experiments performed at magmatic conditions do not necessarily apply to magmatic-hydrothermal systems. Future experiments are needed in order to understand S geochemistry in apatite from hydrothermal deposits.

Acknowledgments

We thank Dr. George Harlow, Curator at the American Museum of Natural History, New York, and Jamie DiPuppo for collecting, and providing the Phillips Mine sample. We thank Owen Neil for assistance in data acquisition and Jeff B. Langman for providing an APS run sulfite standard spectra. We acknowledge the analytical facilities at the American Museum of Natural History (New York, USA), and the University of Michigan (USA). This research used resources of the Advanced Photon Source, a U.S. Department of Energy (DOE) Office of Science User Facility operated for the DOE Office of Science by Argonne National Laboratory under Contract No. DE-AC02-06CH11357. This work was funded by Society of Economic Geologists Student Research Grant 2017, and by the National Science Foundation (NSF grant EAR1524394 to A.S. and A.F.).

References:

Als-Nielsen, J., and McMorrow, D. (2011) Elements of Modern X-ray Physics. John Wiley & Sons, 2nd edition, 434.

Barbarand, J. and Pagel, M. (2001) Cathodoluminescence study of apatite crystals. *American Mineralogist*, 4, 473-484.

Barnes, H. L., and Czamanske, G. K. (1967) Solubilities and transport of ore minerals, in Barnes, H, L., ed., Geochemistry of hydrothermal ore deposits: New York, Holt, Rinehart, and Winston, 334-381.

Barnes, S. J., and Lightfoot, P. C. (2005) Formation of magmatic nickel sulfide deposits and processes affecting their copper and platinum group elements contents. In: Economic Geology 100th Anniversary Volume. Hedenquist, J.W., Thompson, J.F.H., Goldfarb, R.J., Richards, J.P. (eds), 179-213.

Barré, G., Truche, L., Michels, R., Barré, G., Truche, L., and Michels, R. (2015) Sulfur speciation in natural fluid inclusions at elevated temperatures.

Barton, O., and Toulmin, P. (1964) Experimental determination of the reaction chalcopyrite+sulfur=pyrite+bornite from 350 to 500 degrees C. *Economic Geology,* 59, 747–752. doi: https://doi.org/10.2113/gsecongeo.59.5.747.

Beck, L., C. (1842) Mineralogy of New York. Albany, New York.

Betkowski, B., Harlov, D.E., and Rakovan, J. F. (2016) Hydrothermal mineral replacement reactions for an apatite-monazite assemblage in alkali-rich fluids at 300–600 °C and 100 MPa. *American Mineralogist*, 101, 2620–2637. doi: https://doi.org/10.2138/am-2016-5765.

Betts, J. (1997) Anthony's Nose, New York A Review of Three Mineral Localities. *Matrix Magazine.*

Campbell, L. D., and Grauch, I. R. (1977) Ground magnetic, E-mode VLF, and radiometric surveys at Phillips Mine-Camp Smith uranium prospect, Westchester and Putnam Counties, New York. U.S. Geological Survey, Denver, Colorado, 80225. Open File Report 77-780.

Carroll, M. R., and Webster, J. D. (1994) Solubilities of sulfur, noble gases, nitrogen, chlorine, and fluorine in magmas, in Volatiles in Magmas, edited by Carroll, M.R., Holloway, J.R. Rev. Mineral., 30, 231-279.

Carroll, M. R., and Rutherford, M. J. (1988) Sulfur speciation in hydrous experimental glasses of varying oxidation state – results from measured wavelength shifts of sulfur X-rays. *American Mineralogist,* 73, 845–849.

Drouin, D., Couture, R.A., Joly, D., Tastet, X., Aimez, V., and Gauvin, R. (2007) CASINO V2. 42 — A Fast and Easy-to-Use Modeling Tool for Scanning Electron Microscopy and Microanalysis Users. Wiley Periodicals, Inc., 29, 92–101.

Farley, K., Shuster D. I., and Ketcham, R. A. (2011) U and Th zonation in apatite observed by laser ablation ICPMS, and implications for the (U-Th)/He system. *Geochimica et Cosmochimica Acta*, 75, 4515-4530.

Fleet, M. E. (2005) XANES Spectroscopy of sulfur in Earth Materials. *The Canadian Mineralogist*, 43, 1811-1838.

Fontboté, L., Kouzmanov, K., Chiaradia, M., and Pokrovski, G.S. (2017) Sulfide Minerals in Hydrothermal Deposits. *Elements*, 13, 97-103. doi: 10.2113/gselements.13.2.97.

Fiege, A., Holtz, F., Behrens, H., Mandeville, C. W., Shimizu, N., Crede, L. S., and Göttlicher, J. (2015) Experimental investigation of the S and S-isotope distribution between H2 O–S±Cl fluids and basaltic melts during decompression. *Chemical Geology*, 393, 36-54.

Goldoff, B., Webster, J. D. and Harlov, D. E. (2012) Characterization of fluorchlorapatites by

electron probe microanalysis with a focus on-dependent intensity variation of halogens. *American Mineralogist*, 97, 1103-1115.

Götze, J. (2012) Application of cathodoluminescence microscopy and spectroscopy in geosciences. Microsc Microanal, 18, 1270–1284. doi: 10.1017/S1431927612001122

Götze, J., Pltze, M., and Habermann, D. (2001) Origin, spectral characteristics and practical applications of the cathodoluminescence (CL) of quartz - a review. *Mineralogy and Petrology*, 71, 225 - 250.

Gros, K., Słaby, E., Förster, H.J., Michalak, P.P., Munnik, F., Götze, J., and Rhede, D. (2016) Visualization of trace-element zoning in fluorapatite using BSE and CL imaging, and EPMA and μPIXE/μPIGE mapping. *Mineralogy and Petrology*, 110, 809-821. doi:10.1007/s00710-016-0452-4.

Hall, A. J. (1986) Pyrite-pyrrhotine redox reactions in nature. *Mineralogical Magazine*, 50, 223-229.

Harlov, D. E. (2015) Apatite: A fingerprint for metasomatic processes. *Elements*, 11, 171–176.

Harlov, D. E., Andersson U.B., Förster, H.J., Nyström, J.O., Dulski, P., and Broman, C. (2002) Apatite –monazite relations in the Kiirunavaara magnetite – apatite ore, northern Sweden. *Chemical Geology*, 191,47–72.

Harlov, D.E., and Förster, H.J. (2003) Fluid-induced nucleation of (Y + REE)-phosphate minerals within apatite: Nature and experiment. Part II. Fluorapatite. *American Mineralogist*, 88, 1209-1229.

Henning, P. A., Adolfsson, E., and Grins, J. (2000) The chalcogenide phosphate apatites Ca10(PO4)6S, Sr10(PO4)6S, Ba10(PO4)6S and Ca10(PO4)6Se. Zeitschrift für Kristallographie-Crystalline Materials, 215, 105110.

Hughes, J. M., and Rakovan, J. F. (2002) The Crystal Structure of Apatite, Ca5(PO4)3(F,OH,Cl). *Reviews in Mineralogy and Geochemistry*, 48, 1-12.

Hughes, J. M., and Rakovan, J. F. (2015) Structurally robust, chemically diverse: apatite and apatite supergroup minerals. *Elements*, 11, 165–170.

Jugo, P. J., Wilke, M. and Botcharnikov, R.E. (2010) Sulfur K-edge XANES analysis of natural and synthetic basaltic glasses: Implications for S speciation and S content as function of oxygen fugacity. *Geochimica et Cosmochimica Acta*, 74, 5926–5938.

Jugo, P. J. (2009) Sulfur content at sulfide saturation in oxidized magmas. *Geology,* 37, 415–418.

Kalczynski, M. J., and Gates, A. E. (2014) Hydrothermal alteration, mass transfer and magnetite mineralization in dextral shear zones, western Hudson Highlands, New York, United States. *Ore Geology Reviews*, 61, 226 - 247.

Katsura, T., and Nagashima, S. (1974). Solubility of sulfur in some magmas at 1 atmosphere. *Geochimica et Cosmochimica Acta*, 38, 517–531.

Kemp, J. F. (1894) The nickel mine at Lancaster Gap, Pennsylvania, and the pyrrhotite deposits at Anthony's Nose, on the Hudson. *American Institute of Mining, Metallurgical, and Petroleum Engineers*, 24, 620-63.

Kempe, U., and Götze, J. (2002) Cathodoluminescence (CL) behaviour and crystal chemistry of apatite from rare-metal deposits. *Mineralogical Magazine,* 66, 151–172.

Keppler, H. (1999). Experimental evidence for the source of excess sulfur in explosive volcanic eruptions. *Science*, *284*, 1652-1654.

Ketcham, R. (2015) Technical Note: Calculation of stoichiometry from EMP data for apatite and other phases with mixing on monovalent anion sites. *American Mineralogist,*100, 1620–1623.

Kirby, E., Reiners, P.W., Krol, M.A., Whipple, K.X., Hodges, K. V, Farley, K.A., Tang, W., and Chen, Z. (2002) Late Cenozoic evolution of the eastern margin of the Tibetan Plateau: Inferences from 40 Ar / 39 Ar and (U-Th)/ He thermochronology. *Tectonics*, 21.

Kim, Y. J., Konecke, B. A., Fiege, A., Simon, A. C, and Becker, U. (2017) An ab-initio study of sulfur-bearing apatite: Energetics and geometry upon incorporation of sulfur. *American Mineralogist*, 5, 1–45.

Klemic, H., Eric, J.H., McNitt, J.R., and McKeown, F.A. (1959) Uranium in Phillips Mine–Camp Smith area, Putnam and Westchester Counties, New York. In: Contributions to the Geology of Uranium, U.S. Geological Survey Bulletin 1074-E., 165-199.

Konecke, B. A., Fiege, A., Simon, A. C., Parat, F., and Stechern, A. (2017a) Co-variability of S6+, S4+ and S2- in apatite as a function of oxidation state: implications for a new oxybarometer. *American Mineralogist,* 102, 548–557.

Konecke, B. A., Fiege, A., Simon, A. C., and Holtz, F. (2017b) Cryptic metasomatism during late-stage lunar magmatism implicated by sulfur in apatite. *Geology,* 8, 739–742.

Lennie, A. R., and Vaughan, D. J. (1996) Spectroscopic studies of iron sulfide formation and

phase relations at low temperatures. Mineral Spectroscopy: A Tribute to Roger G. Burns, 5.

Liu, Y., and Comodi, P. (1993) Some aspects of the crystal-chemistry of apatites. *Mineralogical Magazine*, 57, 709–719.

Llovet, X., and Galan, G. (2003) Correction of secondary X-ray fluorescence near grain boundaries in electron microprobe analysis: Application to thermobarometry of spinel lherzolites. *American Mineralogist,* 88, 121-130.

Llovet, X., and F. Salvat. (2016) PENEPMA: a Monte Carlo programme for the simulation of X-ray emission in EPMA. IOP Conference Series: Materials Science and Engineering. Vol. 109. No. 1, 012009.

Loveman, M. H. (1911) Geology of the Phillips pyrites mine near Peekskill, New York. *Economic Geology*, 6, 231-246.

Luo, Y., Rakovan, J., Tang, Y., Lupulescu, M., Hughes, J.M., and Pan. Y. (2011) Crystal chemistry of Th in fluorapatite. *American Mineralogist*, 96, 23–33.

Lyons, J. I. (1988) Volcanogenic iron oxide deposits, Cerro de Mercado and vicinity, Durango. *Economic Geology*, 83, 1886–1906.

MacRae, M. C., and Wilson, C. N. (2008) Luminescence Database I- Minerals and Materials. *Microscopy and Microanalysis*, 14, 184 - 204.

Mao, M., Rukhlov, A.S., Rowins, S.M., Spence, J., and Coogan, L.A. (2016) Apatite trace element compositions: A robust new tool for mineral exploration. *Economic Geology,* 111, 1187–1222.

Meinert, L. (1992) Skarn and Skarn deposits. *Geoscience Canada*, 19, 145 - 162. https://journals.lib.unb.ca/index.php/GC/article/view/3773/4287.

Mengason, M., Piccoli, P.M., and Candela, P. (2010) AN EVALUATION OF THE EFFECT OF COPPER ON THE ESTIMATION OF SULFUR FUGACITY (f_{S2}) FROM PYRRHOTITE COMPOSITION. *Economic Geology*, 105, 1163–1169. doi: https://doi.org/10.2113/econgeo.105.6.1163.

Mungall, J.E., Andrews, D.R., Cabri, L.J., Sylvester, P.J., and Tubrett, M. (2005) Partitioning of Cu, Ni, Au, and platinum group elements between monosulfide solid solution and sulfide melt under controlled oxygen and sulfur fugacities. *Geochimica et Cosmochimica Acta*, 69, 4349-4360.

Nilsson, K., and Peach, C. L. (1993). Sulfur speciation, oxidation state, and sulfur concentration in backarc magmas. *Geochimica et Cosmochimica Acta*, *57*, 3807–3813.

Parat, F., and Holtz, F. (2004) Sulfur partitioning between apatite and melt and effect of sulfur on apatite solubility at oxidizing conditions. Contributions to Mineralogy and Petrology, 147, 201–212.

Parat, F., Holtz, F., and Streck, M. J. (2011) Sulfur-bearing magmatic accessory minerals. *Reviews in Mineralogy and Geochemistry*, 73, 285–314.

Parat F., Dungan M., and Streck M. J. (2002) Anhydrite, pyrrhotite and sulfur-rich apatite: tracing the sulfur evolution of an Oligocene andesite (Eagle Mountain, CO, USA). *Lithos,* 64, 63-75.

Paris, E., Giuli, G., Carroll, M. R., and Davoli, I. (2001) The valence and speciation of sulfur in glasses by X-ray absorption spectroscopy. *Canadian Mineralogist*, 39, 331–339.

Peng, G., Luhr, J., and McGee, J. (1997) Factors controlling sulfur concentrations in volcanic apatite. *American Mineralogist*, 82, 1210–1224.

Pokrovski, G. S., and Dubessy, J. (2015) Stability and abundance of the trisulfur radical ion S3 in hydrothermal fluids. *Earth and Planetary Science Letters*, 411, 298–309.

Pokrovski, G. S., and Dubrovinsky, L.S. (2011) The S3 ion is stable in geological fluids at elevated temperatures and pressures. *Science*, 331, 1052–1054.

Piccoli, P. M., and Candela, P. A. (2002) Apatite in igneous systems. *Reviews in Mineralogy and Geochemistry*, 48, 255–292.

Ravel, B., and Newville, M. (2005) ATHENA, ARTEMIS, HEPHAESTUS: Data analysis for X-ray absorption spectroscopy using IFEFFIT. *Journal of Synchrotron Radiation*, 12, 537–541.

Robinson, S. (1825) A Catalogue of American Minerals, with their Localities. Cummings, Hilliard, & Co., Boston, 115.

Rouse, R. C., and Dunn, P. J. (1982) A contribution to the crystal chemistry of ellestadite and the silicate sulfate apatites. *American Mineralogist*, 67, 90–96.

Rye, R. O., and Ohmoto, H. (1974) Sulfur and carbon isotopes in ore genesis: a review. *Economic Geology,* 69, 826–842.

Simon, A. C., and Ripley, E. M. (2011) The role of magmatic sulfur in the formation of ore deposits. *Rev. Mineral. Geochemistry,* 73, 513–578.

Spear, F. S., and Pyle, J. M. (2002) Apatite, Monazite, and Xenotime in Metamorphic Rocks. *Reviews in Mineralogy and Geochemistry,* 48, 293-335.

Streck, M. J., and Dilles, J. H. (1998) Sulfur evolution of oxidized arc magmas as recorded in apatite from a porphyry copper batholith. *Geology*, 26, 523.

Tepper, J., and Kuehner, S. (1999) Complex zoning in apatite from the Idaho batholith: A record of magma mixing and intracrystalline trace element diffusion. *American Mineralogist*, 84, 581–595.

Tröger, L. A., Baberschke, D., Michaelis, K., Grimm, H., and Zschech, U. E. (1992). Full Correction of the Self-absorption in Soft-fluorescence Extended X-ray-absorption Fine Structure. *Physical review. B, Condensed matter,* 46.

Waychunas, G. A. (2002) Apatite luminescence, in Kohn, M.J., Rakovan, J., and Hughes, J.M., eds., Phosphates: Geochemical, Geobiological, and Materials Importance. *Reviews in Mineralogy and Geochemistry*, 48, 701–742.

Wallace, P. J., and Carmichael, I. (1994) S speciation in submarine basaltic glasses as determined by measurements of SKa X-ray wavelength shifts. *American Mineralogist*, 79, 161 – 167.

Webster, J. D., and Piccoli, P. M. (2015) Magmatic apatite: A powerful, yet deceptive, mineral. *Elements*, 11, 177–182.

Williams-Jones, A. E., and Heinrich, C. A. (2005) Vapor transport of metals and the formation of magmatic-hydrothermal ore deposits. In: Economic Geology 100th Anniversary Volume. Hedenquist JW, Thompson JFH, Goldfarb RJ, Richards JP (eds) 1287-1312.

Wilke, M., Jugo, P. J., Klimm, K., Susini, J., Botcharnikov, R., Kohn, S.C. and Janousch, M. (2008) The origin of S4+ detected in silicate glasses by XANES. *American Mineralogist*, 93, 235–240.

Wolf, M. B., and London, D. (1995) Incongruent dissolution of REE- and Sr-rich apatite in peraluminous granitic liquids: differential apatite, monazite, and xenotime solubilities during anatexis. *American Mineralogist*, 80, 765-775.

Wojdyr, M. (2010) Fityk: A general-purpose peak fitting program. *Journal of Applied Crystallography,* 43, 1126–1128.

Wood, S, A., Crerar, D, A., and Borcsik, M. P. (1978) Solubility of the assemblage

pyrite-pyrrhotite-magnetite-sphalerite-galena-gold-stibnite-bismuthinite-argentite-molybdenite in H2O-NaCl-CO2 solutions from 200 to 350 °C. *Economic Geology*, 82, 1867-1867.

Wood, S. A., and Samson, I. M. (1998) Solubility of Ore Minerals and Complexation of Ore Metals in Hydrothermal Solutions. Techniques in Hydrothermal Ore Deposits Geology, Richards, J, P., Larson, P, B. doi: https://doi.org/10.5382/Rev.10.02.

Zajacz, Z., Seo, J. H., Candela, P. A., Piccoli, P. A., and Tossell, J. A. (2011) The solubility of copper in high-temperature magmatic vapors: a quest for the significance of various chloride and sulfide complexes. *Geochimica et Cosmochimica Acta*, 75, 2811-2827.

Zajacz, Z., Candela, P. A., Piccoli, P. M., Wälle, M., and Sanchez-Valle, C. (2012) Gold and copper in volatile saturated mafic to intermediate magmas: Solubilities, partitioning, and implications for ore deposit formation. *Geochimica et Cosmochimica Acta*, 91, 140-159. doi:10.1016/j.gca.2012.05.033.

Zodac, P. (1933) The Anthony's Nose Pyrrhotite Mine. Rocks and Minerals, 8, 61-76.

Figure Captions

Fig. 1. Location of the Phillips Mine, New York, U.S.A. 41.3256° N, 73.9514° W.

Fig. 2. The oxidation states of S in apatite represented by XANES normalized spectra. The dotted lines are in-house (APS) XANES spectra of S-bearing reference compounds with known oxidation states; bottom solid lines are S in apatite from this study **A.** The S^{1-} (peak position 2471 eV) in both pyrite (in-house standard from APS) and in the apatite (selected spectra is from Transect 4). **B.** The S^{2-} broad and sharp peaks (position 2476 eV; 2470 eV) in pyrrhotite standard (in-house standard from APS) and in apatite (spectra shown from Fig. 3E; Transect 1). A S^{6+} peak also exists (2482 eV) pointing to the location of the transect within the apatite only. **C.** First top dotted line spectra represent the sodium sulfite in-house standard for S^{4+}, and the second dotted line the clear double-sided adhesive tape, used as the S^{6+} standard (2478 eV; 2482 eV; selected spectra is from Transect 4 in Fig. 4).

Fig. 3. BSE and CL images of apatite grain A. **A.** BSE image of entire apatite (Ap) grain A with large pyrrhotite (Po) inclusion. **B.** BSE image of pyrrhotite with surrounding apatite. **C.** Annotated BSE image showing pyrrhotite (Po), monazite (Mnz; ([REE]PO_4), REE-rich vein, and euhedral pyrite (Py) in the apatite (Ap). **D.** CL image shows blue-violet-luminescence of grain A with complex zoning; EPMA beam traces are visible for transect 1 **E.** CL image with five EPMA line transects (blue dotted arrows), starting in the pyrrhotite and ending in the apatite. The two XANES transects are marked by red dotted arrows.

Fig. 4. BSE images and CL images of apatite grain B. **A.** Overview BSE image of ~⅓ of grain B. **B.** BSE image focused on area of study. **C.** Annotated BSE image; showing monazite (Mnz), magnetite (Mt), pyrite (Py), ferroan carbonate (Cb), pyroxene (Pyx), and secondary phases in the apatite (Ap). **D**. CL image shows the blue-violet-luminescent of grain B with complex zoning; EPMA beam traces are visible for all four transects. **E.** CL image with four EPMA line transects (blue dotted arrow), starting near the multi-phase inclusion. The two XANES transects are marked by red dotted arrows.

Fig. 5. CL image and WDS element maps collected on apatite grain A. **A.** CL image collected near the large pyrrhotite inclusion in apatite grain A. **B.** Zoomed in CL image. **C.** WDS map of Ce. **D.** WDS map of Cl. **E.** Color scale ranges from low (blue) to high (orange) indicating relative concentrations of S in the WDS map.

Fig. 6. EPMA transects collected in grain A (Fig. 3E) away from pyrrhotite and into the apatite (data listed in supplementary Table S4). Dotted line represents EPMA limit of detection. The error bars indicate the 2σ standard deviation of the measured values. **A.** Transect 1; 0-26 μm on pyrrhotite (results not displayed), 26-80 μm on apatite. The first point of transect 1 may be slightly affected by secondary fluorescence produced by the adjacent pyrrhotite. **B.** Transect 2; 0-13 μm on pyrrhotite, 13-93 μm on apatite. **C.** Transect 3; 0-20 μm on pyrrhotite, 20-94 μm on apatite. **D.** Transect 4; 0-8 μm on pyrrhotite; 8-75 μm on apatite. The first point of transect 4 may be slightly affected by secondary fluorescence produced by the adjacent pyrrhotite. **E.** Transect 2 (Ce + La) concentrations in apatite. **F.** Transect 5; 0-5 μm on pyrrhotite, 15-91 μm on apatite. Transect 1 was conducted in a different EPMA session than transects 2-5 (Table S4), which is

reflected in different respected detection limits.

Fig. 7. EPMA line transects collected in grain B (Fig. 4E) away from the multi-phase inclusion into the apatite (data listed in supplementary Table S4). Dotted line represents EPMA limit of detection in apatite. The standard deviation 2σ error bars are displayed. **A.** Transect 6; 0-29 μm on pyrite (results not displayed); 30-92 μm on apatite. **B.** Transect 7; 0-10 μm on pyrite (results not displayed); 11-104 μm on apatite. The first two points on apatite a probably affected by secondary fluorescence, resulting in artificially high S contents. **C.** Transect 8; line collected away from the carbonate and into the apatite. 0-20 μm on carbonate (results not displayed); 20-102 μm on apatite. **D**. Transect 9; line collected away from the carbonate and into the apatite. 0-32 μm on carbonate (results not displayed); 32-98 μm on apatite.

Fig. 8. Ternary diagram identifies the apatite of the Phillips Mine as fluorapatite. (Supplemental Data Table S1 and S4).

Fig. 9. Histograms for S contents and oxidation states. **A.** Histogram of S content measured in the apatite grains. **B.** Histograms of the $S^{6+}/\sum S$ integrated peak area ratio results (including the assumed 0 values for S^{1-}).

Fig. 10. Results from S XANES and EPMA line transects. Only results from EPMA transects adjacent and parallel to the XANES transects are displayed. **A,C,E,G.** Normalized XANES spectra from the four line transect collected on the Phillips Mine apatite grains. Each spectrum displayed represents a single location away from the apatite-pyrrhotite interface (**A,C**) or the

apatite-carbonate interface (**E, G**). **A, C.** Transects collected away from the pyrrhotite, into the apatite, show S oxidation ranges from mostly sulfate to mostly sulfide in the apatite. **E, G.** Transects collected away from carbonate and into apatite reveal the presence of S^{1-}, S^{4+} and S^{6+} in variable proportions. All XANES analyses were conducted at a sufficient distance away from the apatite-pyrrhotite and apatite-pyrite such that secondary fluorescence did not occur. **B, D, F, H.** The integrated peak area ratio of $S^{6+}/\sum S_{area}$ plotted against the distance to the pyrrhotite (B, D) and ferroan carbonate (F, H). Monosulfide (S^{1-}) peaks represented as white diamonds and were not included in the $S^{6+}/\sum S_{area}$ ratio calculation, thus we set it to zero (i.e., all sulfide). **D.** XANES Transect 2 is located between EPMA Transects 1 and 2 (Fig. 3E). **H.** XANES Transect 4 is located parallel to EPMA Transect 7, and within ±10 μm of each other. The 2σ standard error bars are displayed; error bars not visible when smaller than symbol size.

Fig. 11. Schematic model illustrating the formation of the Phillips Mine apatite, its texture and its inclusions.

(A) Reduced hydrothermal S-bearing fluid

(B) Iron oxides and iron sulfides crystallized from a hydrothermal fluid. Apatite started to crystallize. The fluid alters existing hornblende to pyroxene.

(C – D) Apatite continued to grow and incorporated the existing phases.

(E) Apatite is altered by a relatively oxidized hydrothermal fluid in the presence of sulfides. This results in the formation of S-poor apatite where S is dominantly present as S^{2-} in the fluid and the apatite structure. Pyrrhotite then begins to break down (represented in alteration of Po in grain A). The S^{1-} regions in the apatite (grain B) near the pyrite form. Cracks cutting through the apatite are formed by alteration.

(F) Hydrothermal oxidized S-bearing fluids percolates through apatite owing to the nano- and micron-scale porosity of apatite, and cause dissolution-reprecipitation of apatite. This metasomatism results in REE-rich veins, monazite, and zones with S^{4+} and S^{6+} as identified by XANES. This fluid is also characterized by a higher Cl/F ratios when compared to the primary fluid of stage A. Thus, the re-precipitated apatites are comparably Cl-enriched (Fig. 4), considering the apatite preferentially incorporates F over Cl (Harlov, 2015). Ferroan carbonate may have formed during stages E/F as a result of alteration (Meinert, 1992).

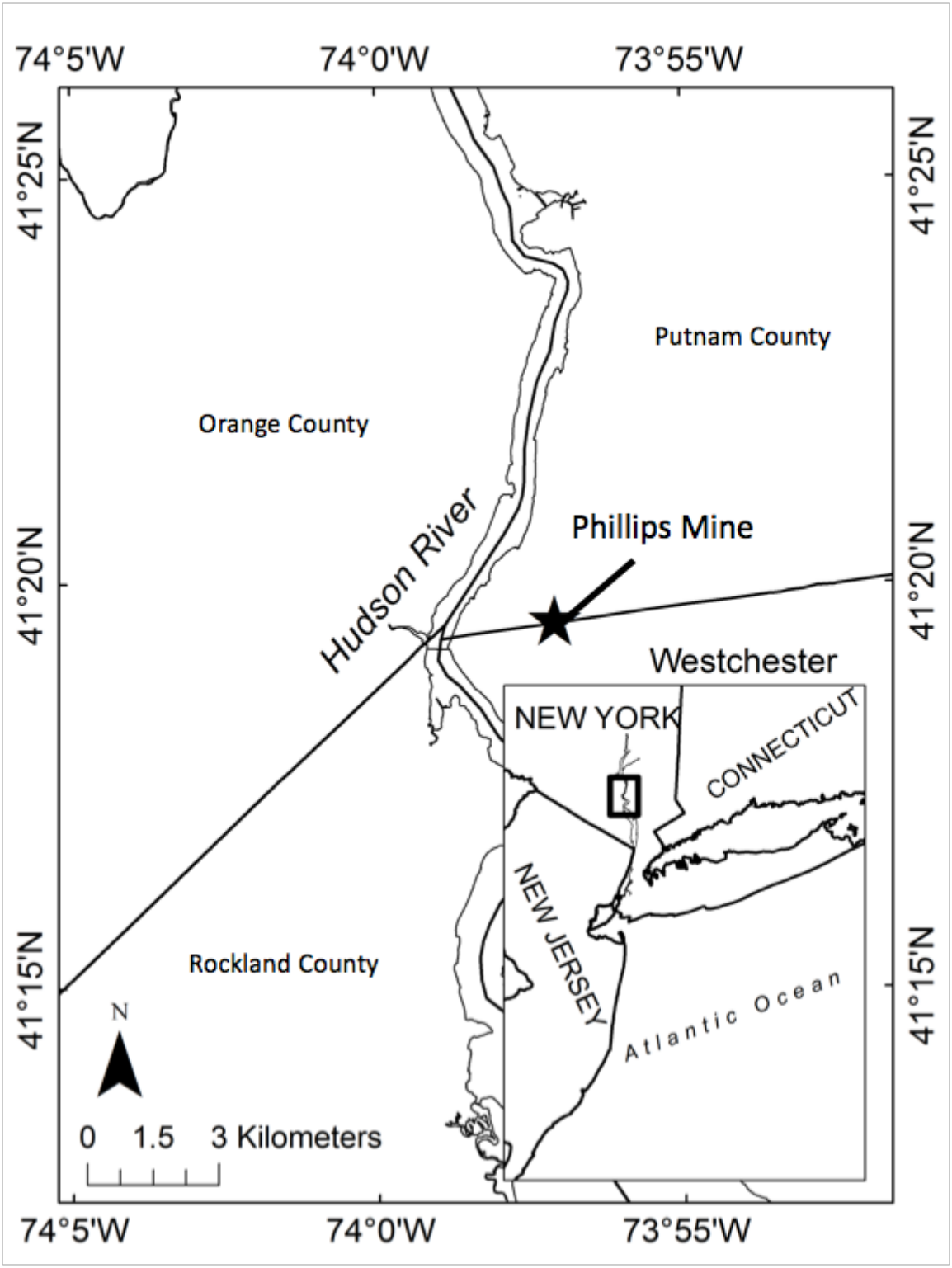
74°5'W
74°0'W
73°55'W
41°25'N
41°20'N
41°15'N
Putnam County
Orange County
Hudson River
Phillips Mine
Westchester
NEW YORK
CONNECTICUT
NEW JERSEY
Atlantic Ocean
Rockland County
N
0 1.5 3 Kilometers

Fig. 1

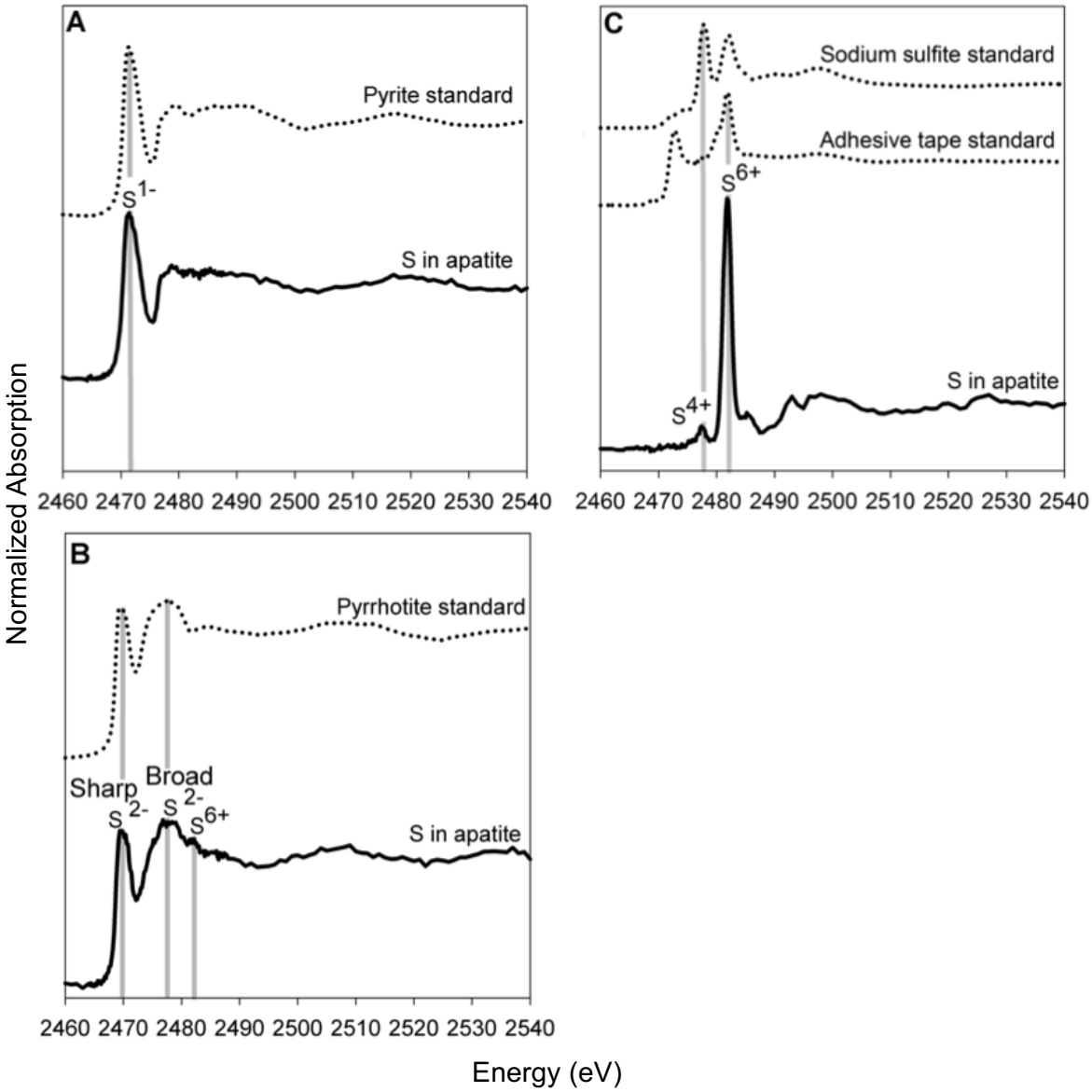
A
Pyrite standard
S 1-
S in apatite
C
Sodium sulfite standard
Adhesive tape standard
S 6+
S 4+
S in apatite
B
Pyrrhotite standard
Sharp
Broad
S 2-
S 2-
S 6+
S in apatite
Normalized Absorption
2460 2470 2480 2490 2500 2510 2520 2530 2540
Energy (eV)

Fig. 2

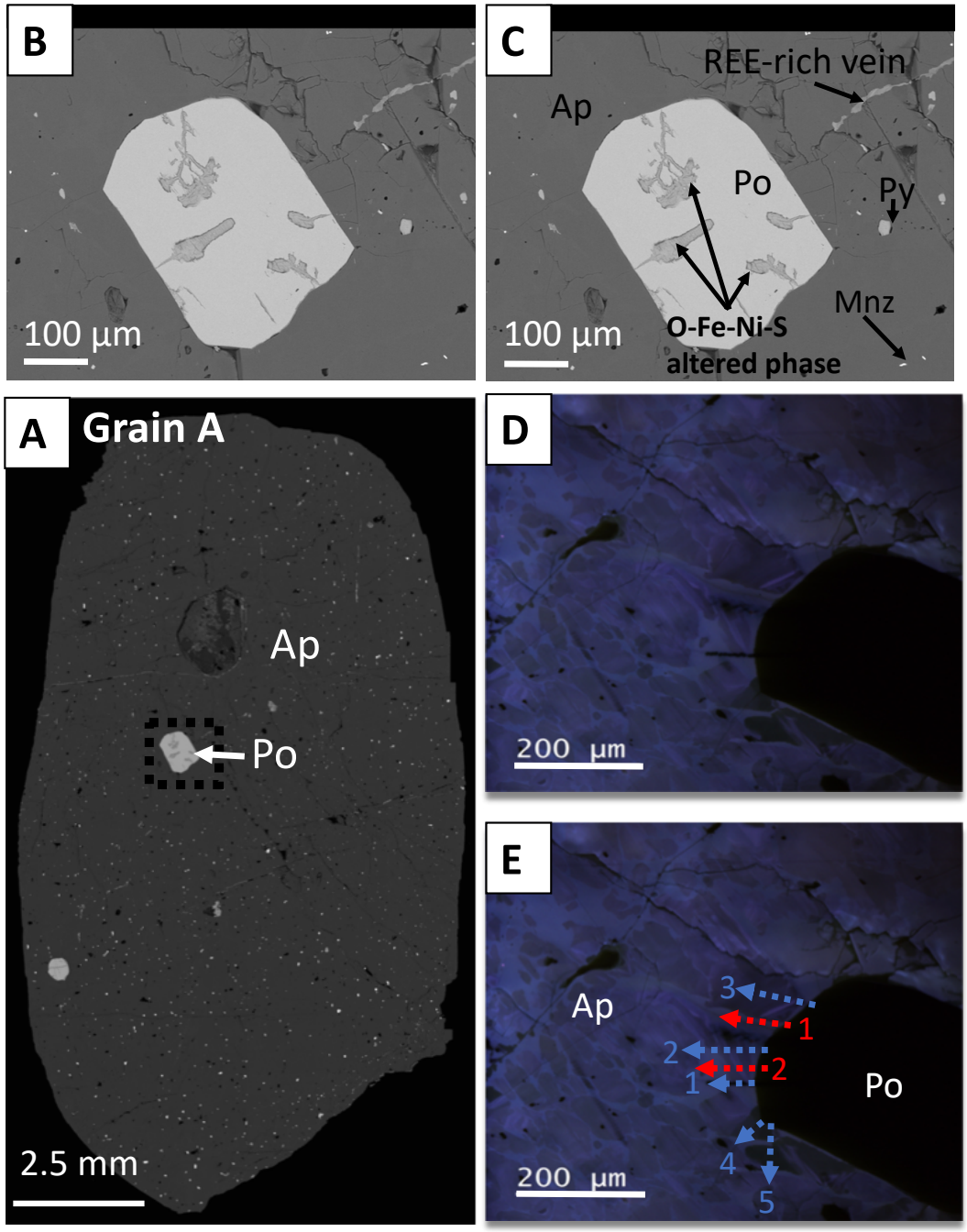
B
100 µm
C
REE-rich vein
Ap
Po
Py
Mnz
O-Fe-Ni-S
altered phase
100 µm
A
Grain A
Ap
Po
2.5 mm
D
200 µm
E
Ap
Po
3
1
2
2
1
4
5
200 µm

Fig. 3

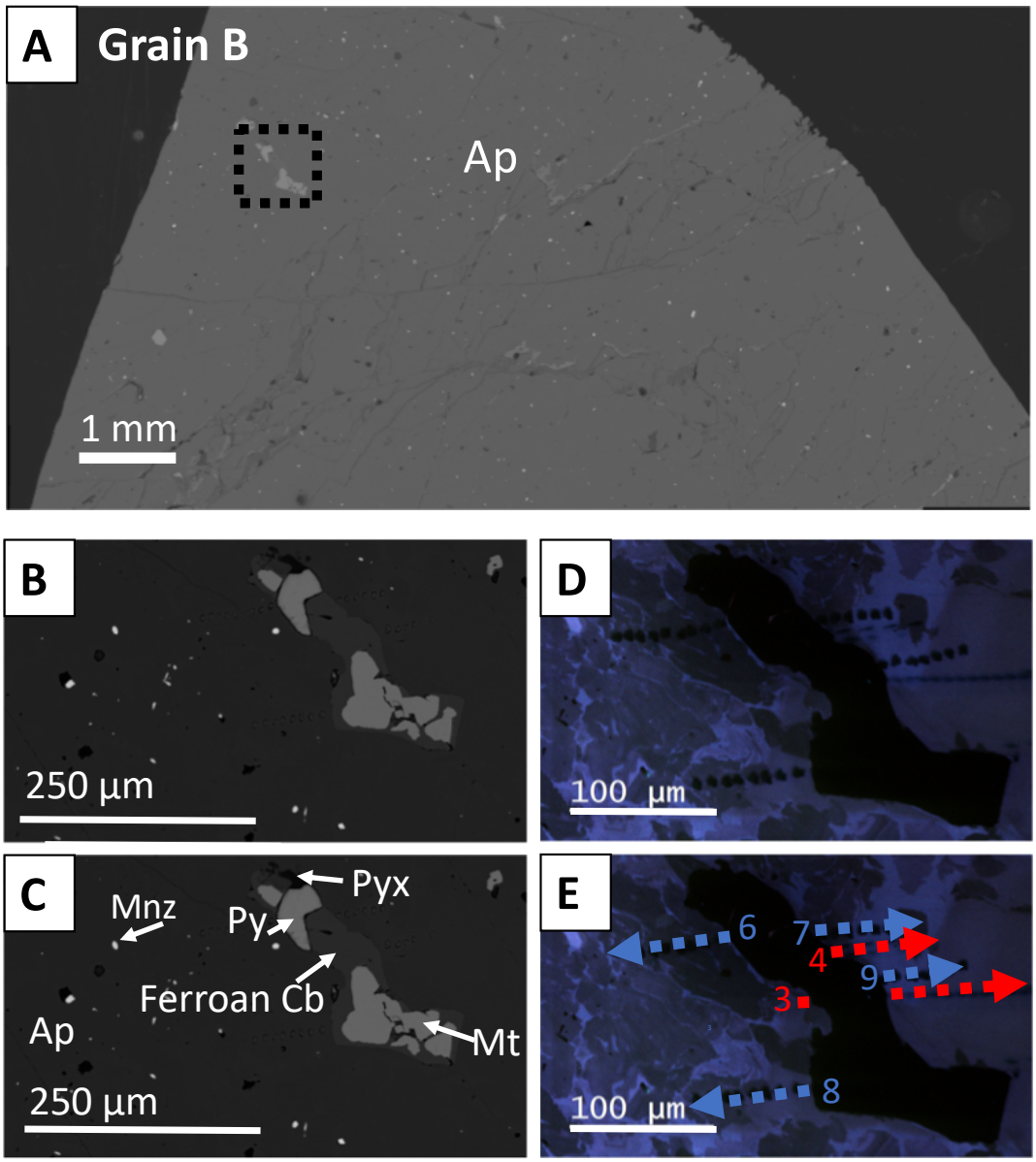
A
Grain B
Ap
1 mm
B
250 µm
D
100 µm
C
Mnz
Py
Pyx
Ferroan Cb
Ap
Mt
250 µm
E
6
7
4
9
3
8
100 µm

Fig. 4

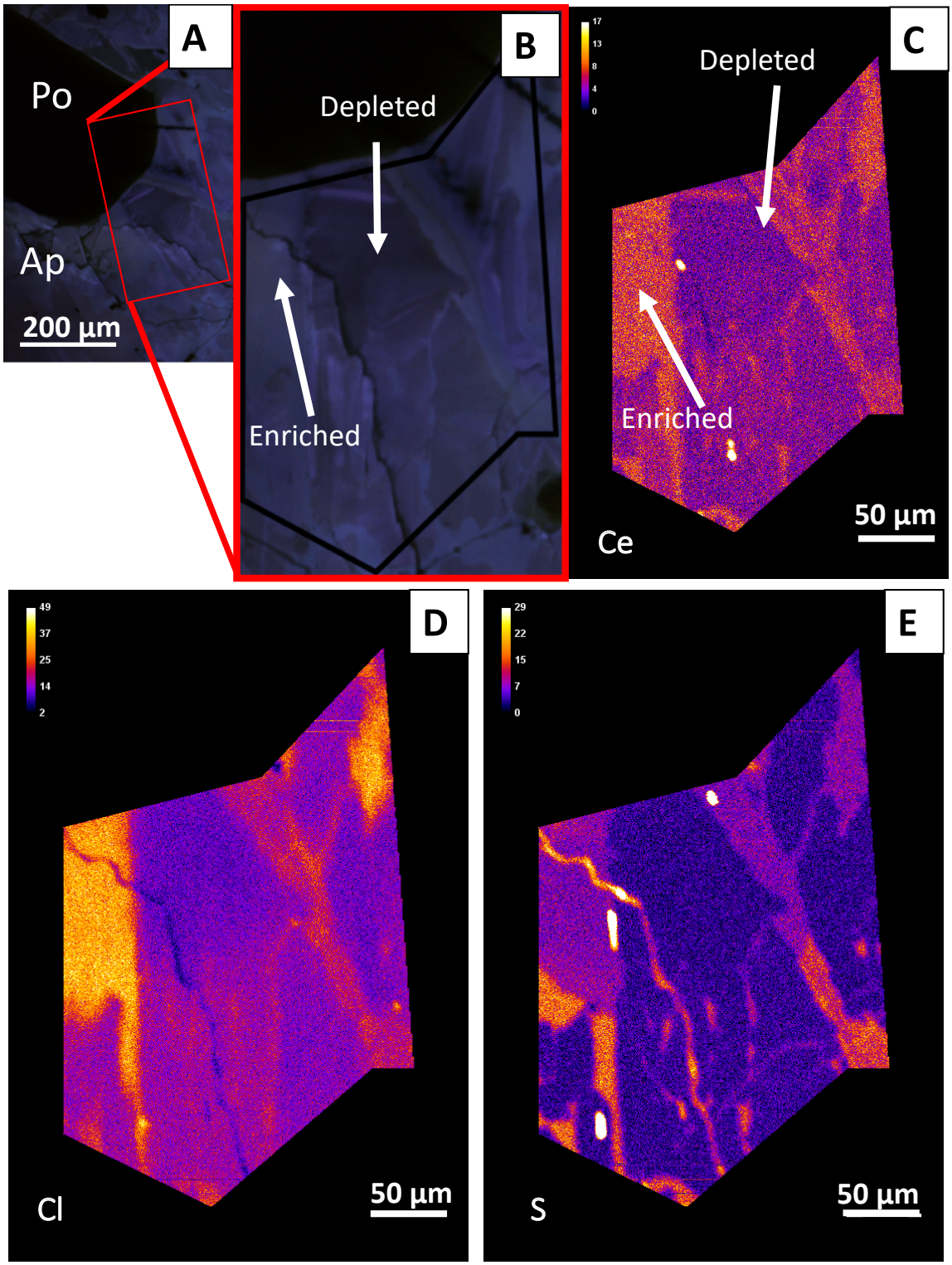
A
Po
Ap
200 µm
B
Depleted
Enriched
C
17
13
8
4
0
Depleted
Enriched
Ce
50 µm
D
49
37
25
14
2
Cl
50 µm
E
29
22
15
7
0
S
50 µm

Fig. 5

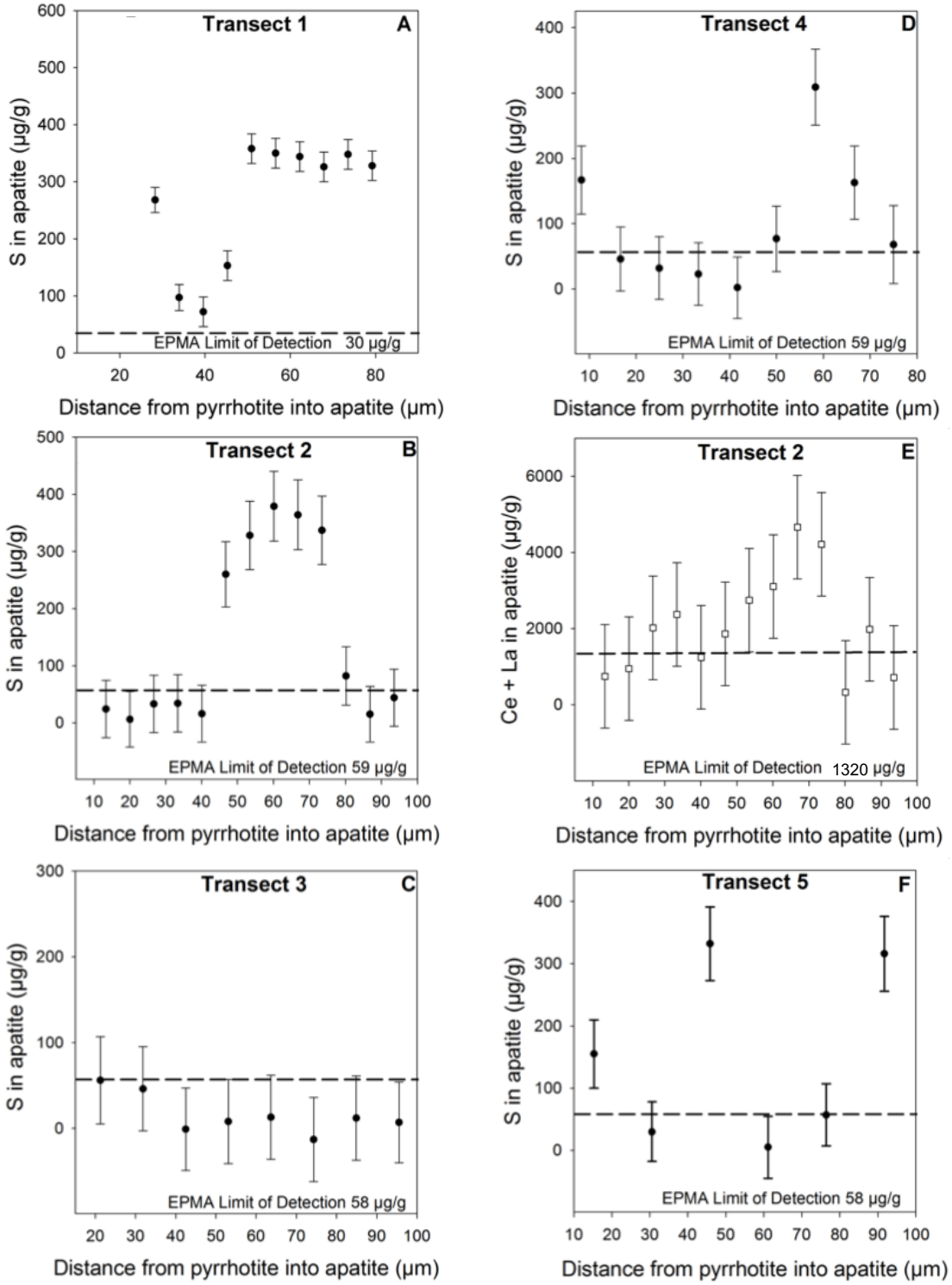
Transect 1
A
S in apatite (µg/g)
EPMA Limit of Detection 30 µg/g
Distance from pyrrhotite into apatite (µm)
Transect 4
D
S in apatite (µg/g)
EPMA Limit of Detection 59 µg/g
Distance from pyrrhotite into apatite (µm)
Transect 2
B
S in apatite (µg/g)
EPMA Limit of Detection 59 µg/g
Distance from pyrrhotite into apatite (µm)
Transect 2
E
Ce + La in apatite (µg/g)
EPMA Limit of Detection 1320 µg/g
Distance from pyrrhotite into apatite (µm)
Transect 3
C
S in apatite (µg/g)
EPMA Limit of Detection 58 µg/g
Distance from pyrrhotite into apatite (µm)
Transect 5
F
S in apatite (µg/g)
EPMA Limit of Detection 58 µg/g
Distance from pyrrhotite into apatite (µm)

Fig. 6

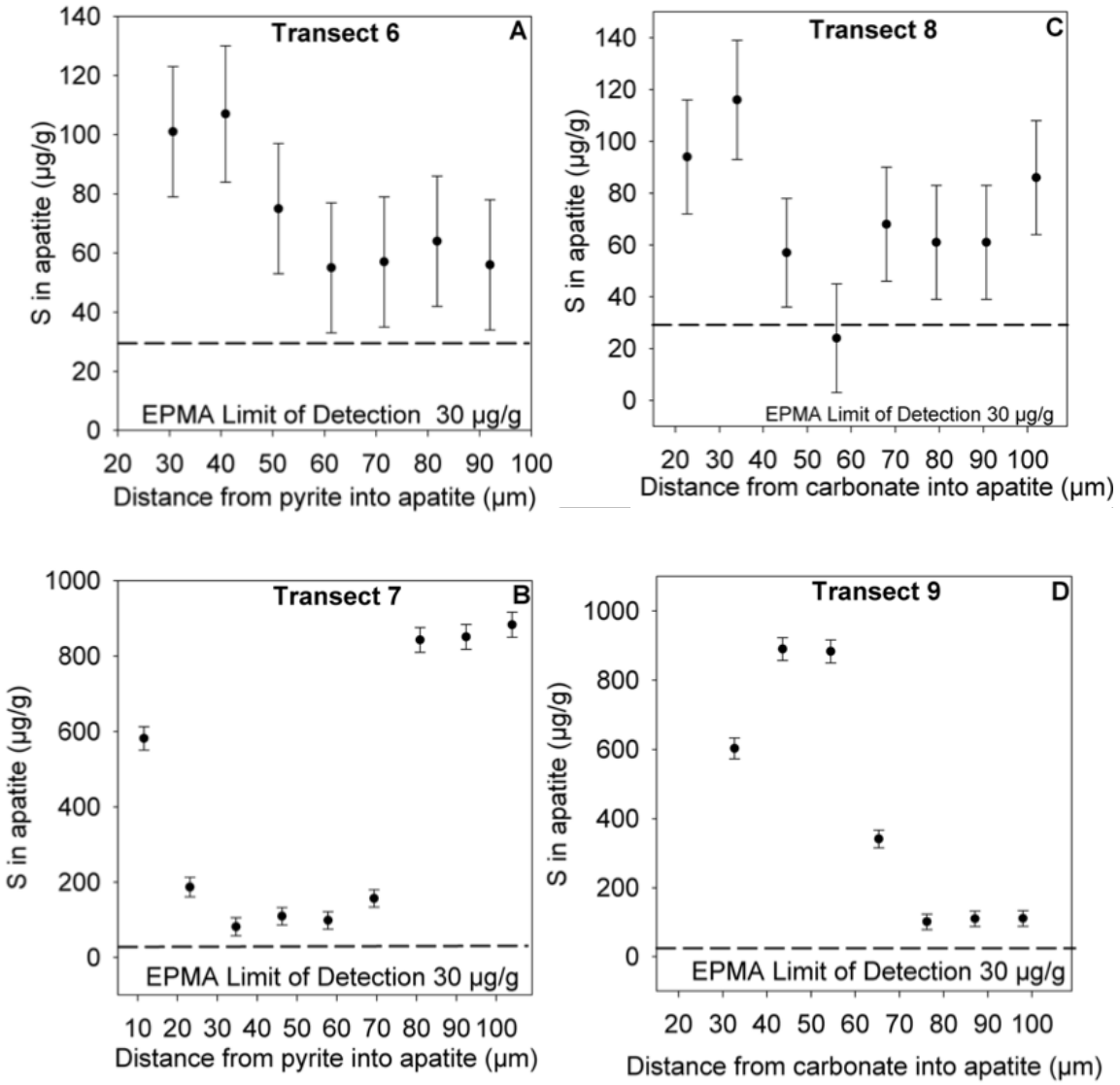
Transect 6
A
S in apatite (µg/g)
EPMA Limit of Detection 30 µg/g
Distance from pyrite into apatite (µm)
Transect 8
C
S in apatite (µg/g)
EPMA Limit of Detection 30 µg/g
Distance from carbonate into apatite (µm)
Transect 7
B
S in apatite (µg/g)
EPMA Limit of Detection 30 µg/g
Distance from pyrite into apatite (µm)
Transect 9
D
S in apatite (µg/g)
EPMA Limit of Detection 30 µg/g
Distance from carbonate into apatite (µm)

Fig. 7

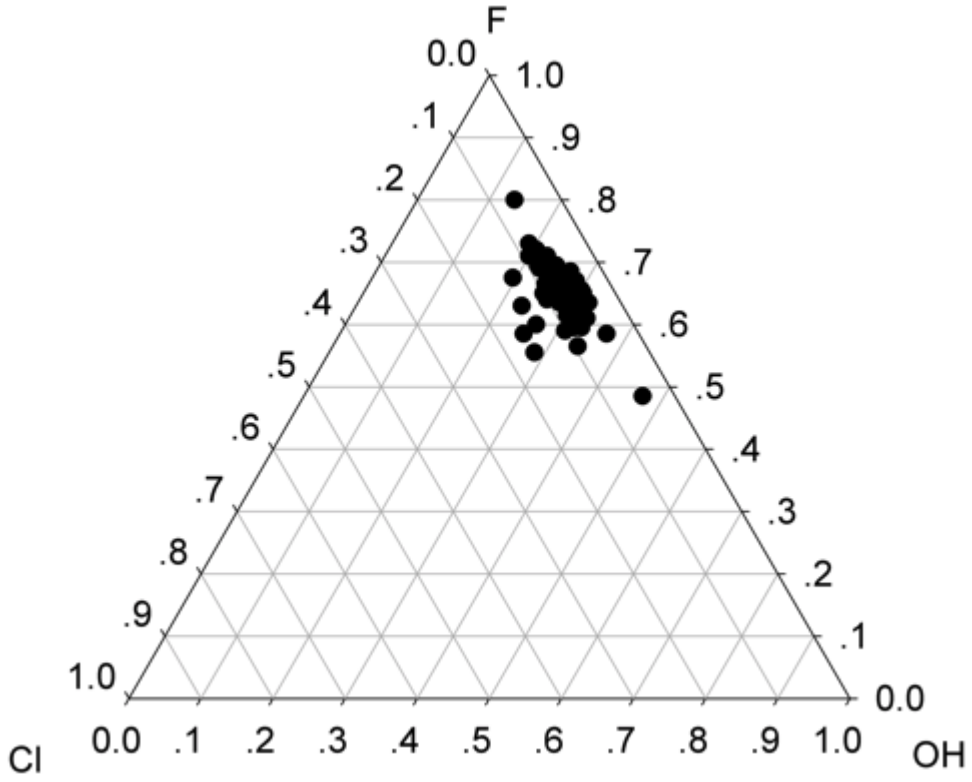

Fig. 8

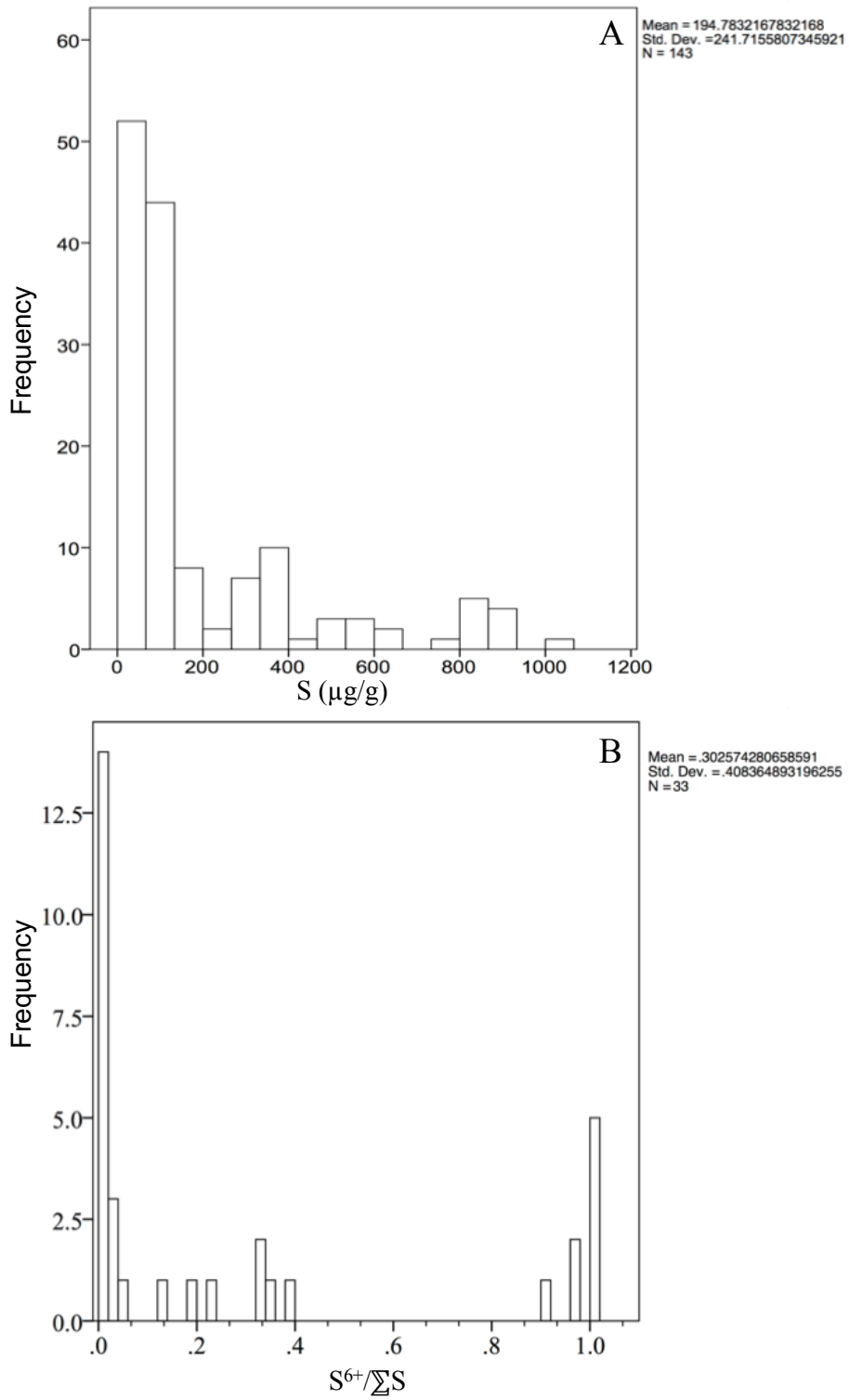
A
Mean = 194.7832167832168
Std. Dev. =241.7155807345921
N = 143
Frequency
S (µg/g)
B
Mean =.302574280658591
Std. Dev. =.408364893196255
N =33
Frequency
S6+/∑S

Fig. 9

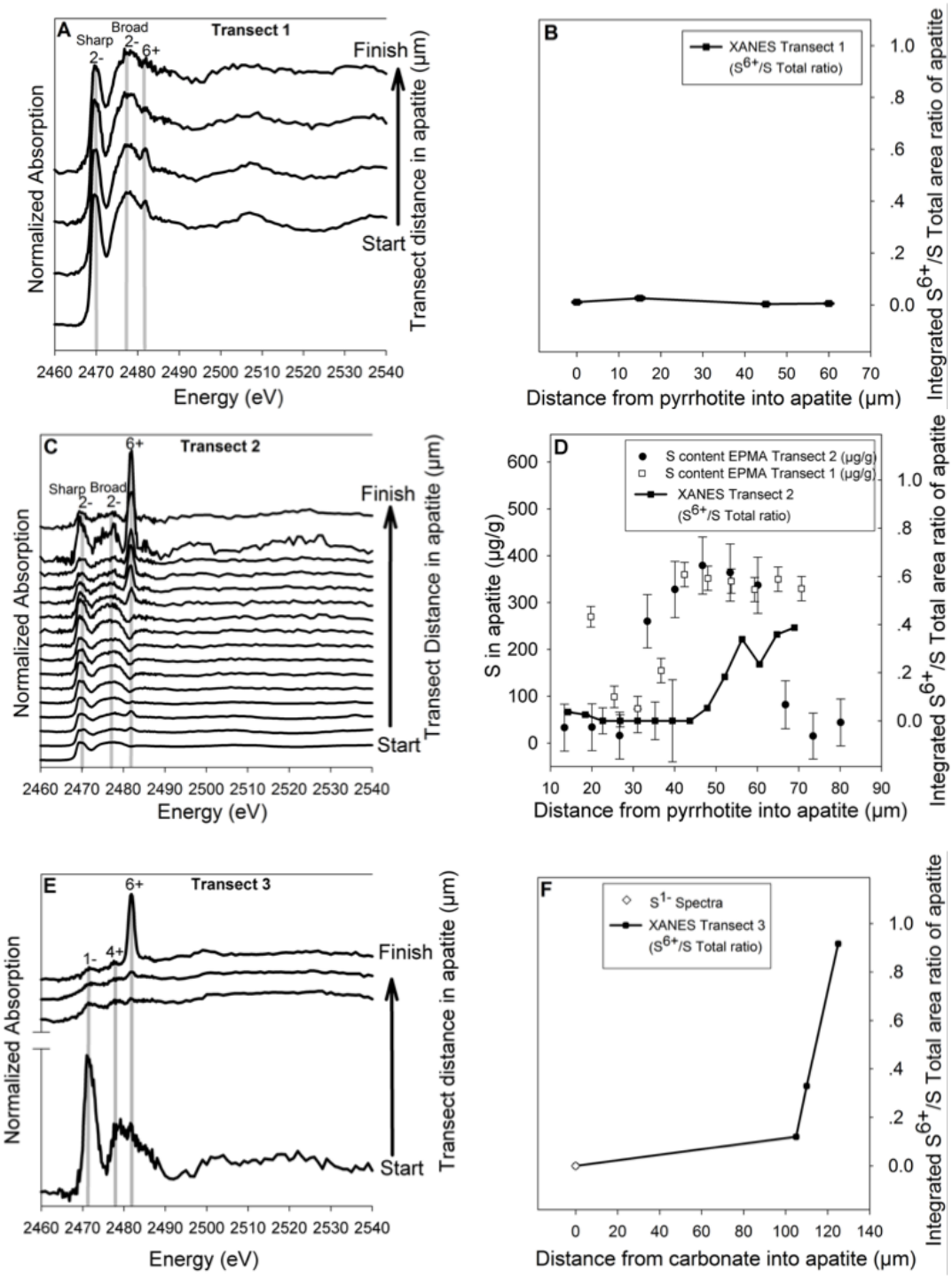
A
Transect 1
Sharp 2-
Broad 2-
6+
Finish
Start
Normalized Absorption
Transect distance in apatite (µm)
Energy (eV)
B
XANES Transect 1 (S6+/S Total ratio)
Distance from pyrrhotite into apatite (µm)
Integrated S6+/S Total area ratio of apatite
C
Transect 2
Sharp 2-
Broad 2-
6+
Finish
Start
Normalized Absorption
Transect Distance in apatite (µm)
Energy (eV)
D
S content EPMA Transect 2 (µg/g)
S content EPMA Transect 1 (µg/g)
XANES Transect 2 (S6+/S Total ratio)
S in apatite (µg/g)
Distance from pyrrhotite into apatite (µm)
Integrated S6+/S Total area ratio of apatite
E
Transect 3
1-
4+
6+
Finish
Start
Normalized Absorption
Transect distance in apatite (µm)
Energy (eV)
F
S1- Spectra
XANES Transect 3 (S6+/S Total ratio)
Distance from carbonate into apatite (µm)
Integrated S6+/S Total area ratio of apatite

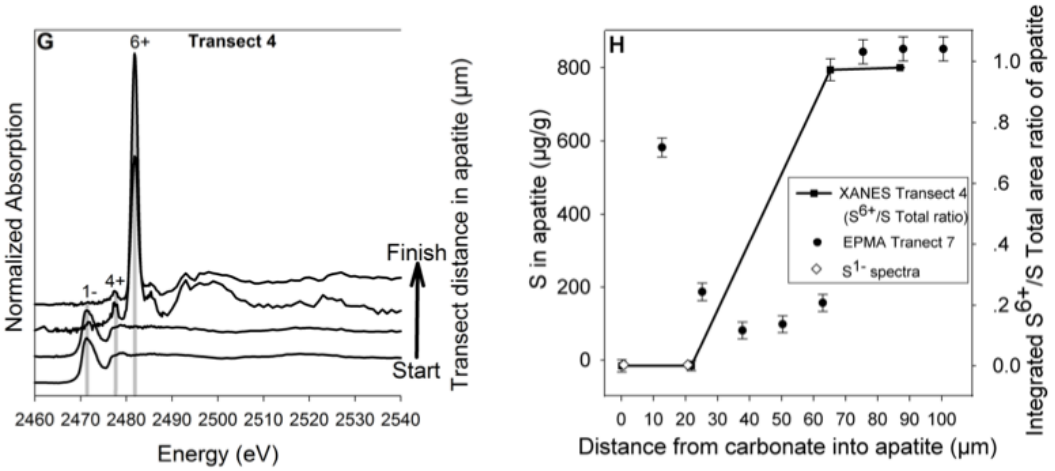
G
Transect 4
6+
1-
4+
Finish
Start
Normalized Absorption
Transect distance in apatite (µm)
2460 2470 2480 2490 2500 2510 2520 2530 2540
Energy (eV)
H
S in apatite (µg/g)
Integrated S6+/S Total area ratio of apatite
XANES Transect 4
(S6+/S Total ratio)
EPMA Tranect 7
S1- spectra
Distance from carbonate into apatite (µm)

Fig. 10

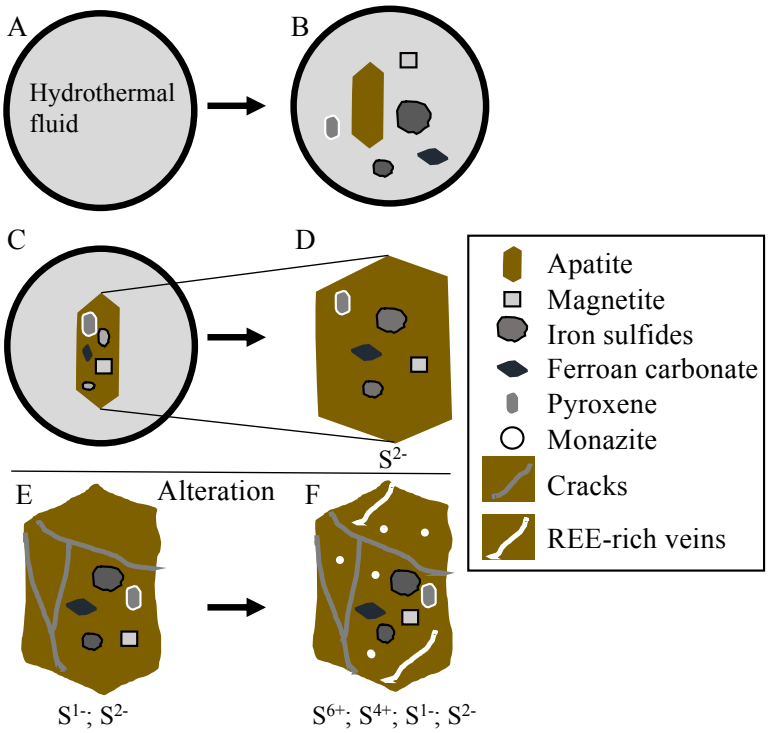
A
Hydrothermal fluid
B
C
D
S^{2-}
Apatite
Magnetite
Iron sulfides
Ferroan carbonate
Pyroxene
Monazite
Cracks
REE-rich veins
E
Alteration
F
S^{1-}; S^{2-}
S^{6+}; S^{4+}; S^{1-}; S^{2-}

Fig. 11

Supplementary:

S1. Compilation of S *K*-edge XANES spectra of S-bearing reference materials with varying S oxidation states in apatite (from S^{2-} to S^{6+}).

S2. Additional BSE images show apatite A and apatite B with affiliated EPMA transects locations (A1 and B1) represented in white dotted arrows (Supplementary Data Table S2).

S3. Additional BSE images of grain A and B. **A.** BSE image of the large pyrrhotite inclusion in grain A (Supplementary Data Table S2). EPMA points (in red) within the Fe - Ni - O - S altered phase and line transects (33-34) within the pyrrhotite matrix. **B.** The BSE image of the multi-phase inclusion (pyrite - ferroan carbonate - pyroxene) in grain B and EPMA points (Table S2).

S4. Results of CASINO software Monte Carlo simulations with setting of 15 kV, FeS sample (Drouin et al. 2007). **A.** $\Phi(\rho Z)$ (ionization distribution function) curve of FeS sample simulated at 15 kV. In terms of depth, there is no contribution to the overall characteristic S X-ray measurement from below 1500 nm. **B.** X-ray intensity as a function of radial distance (nm) from electron beam, simulated at 15 kV. Laterally, there is ~0 contribution to the overall X-ray measurement from outside 500nm from the center of the beam, with the most significant contribution from within ~250 nm. Sulfur X-rays that are generated by the beam are coming from not farther than 250-500 nm from the center of the beam, and not deeper than 1000-1500 nm in the sample.

S5. Unnormalized S XANES spectra. **A, B.** Pyrrhotite and Pyrite intensity (raw x-ray counts) are orders of magnitude higher than the S in apatite intensity, where intensity is related to S concentration. This change in intensity further supports the location of the analysis within the apatite.

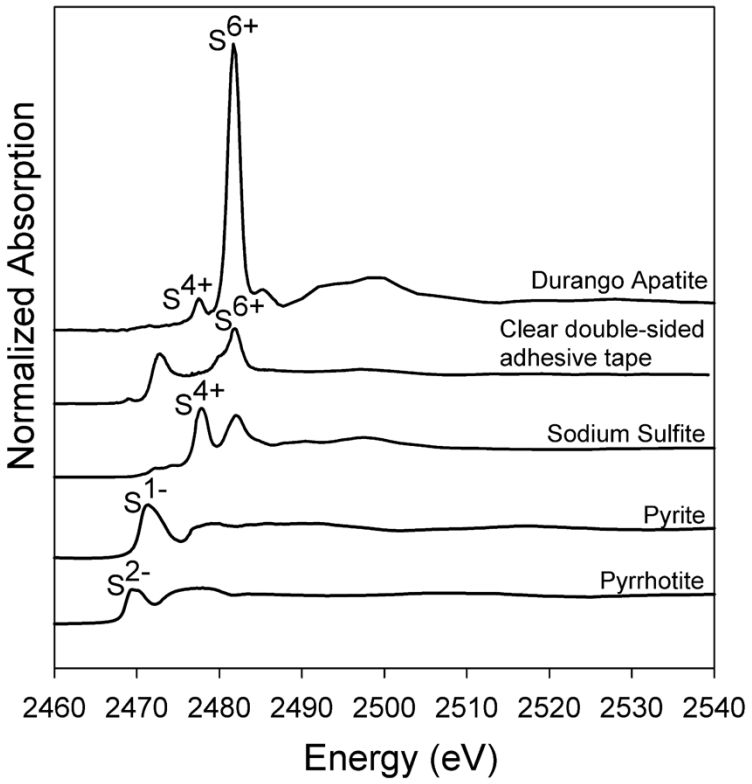
S6+
S4+
S6+
S4+
S1-
S2-
Durango Apatite
Clear double-sided adhesive tape
Sodium Sulfite
Pyrite
Pyrrhotite
Normalized Absorption
2460 2470 2480 2490 2500 2510 2520 2530 2540
Energy (eV)

S1.

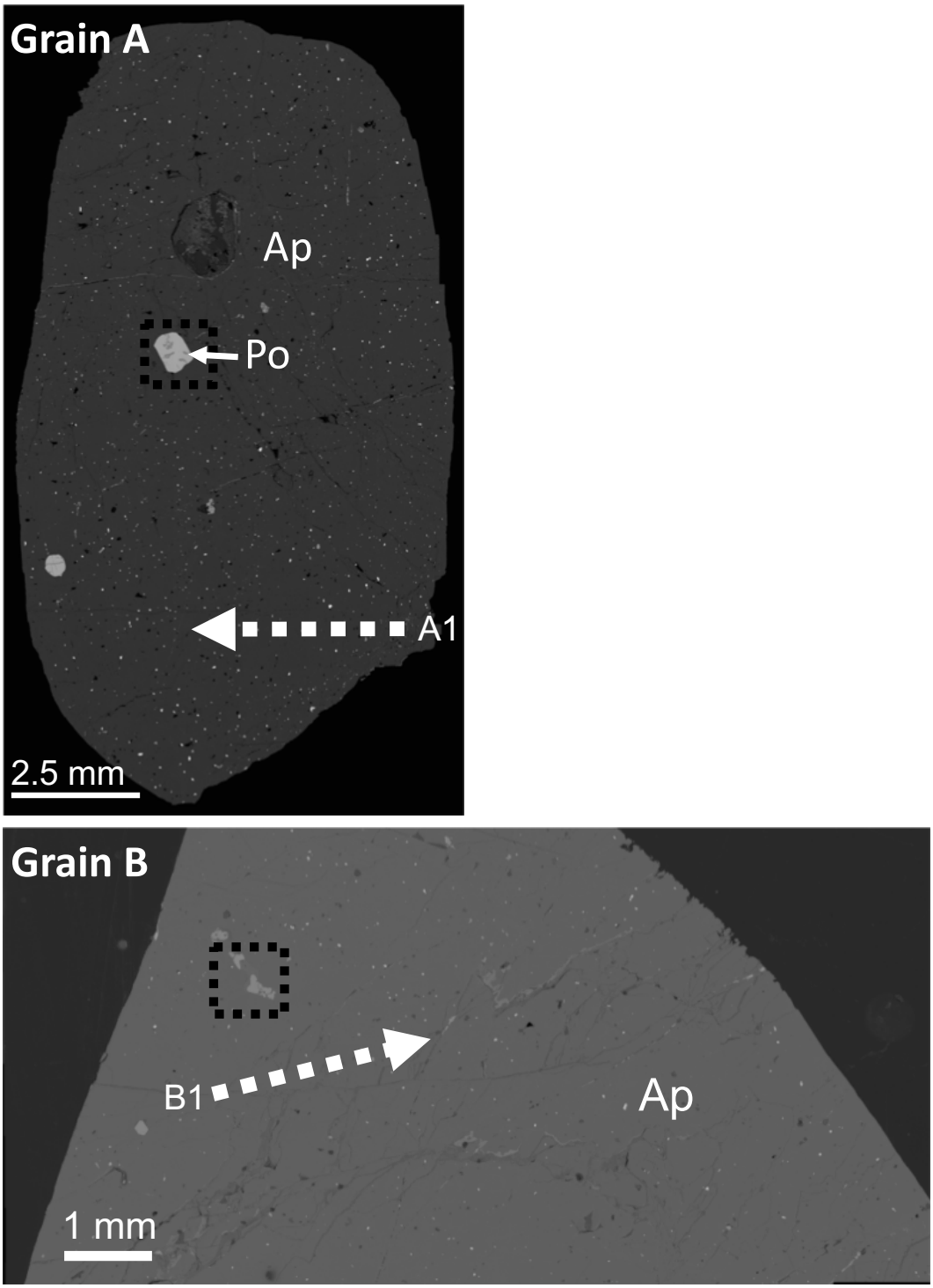

S2.

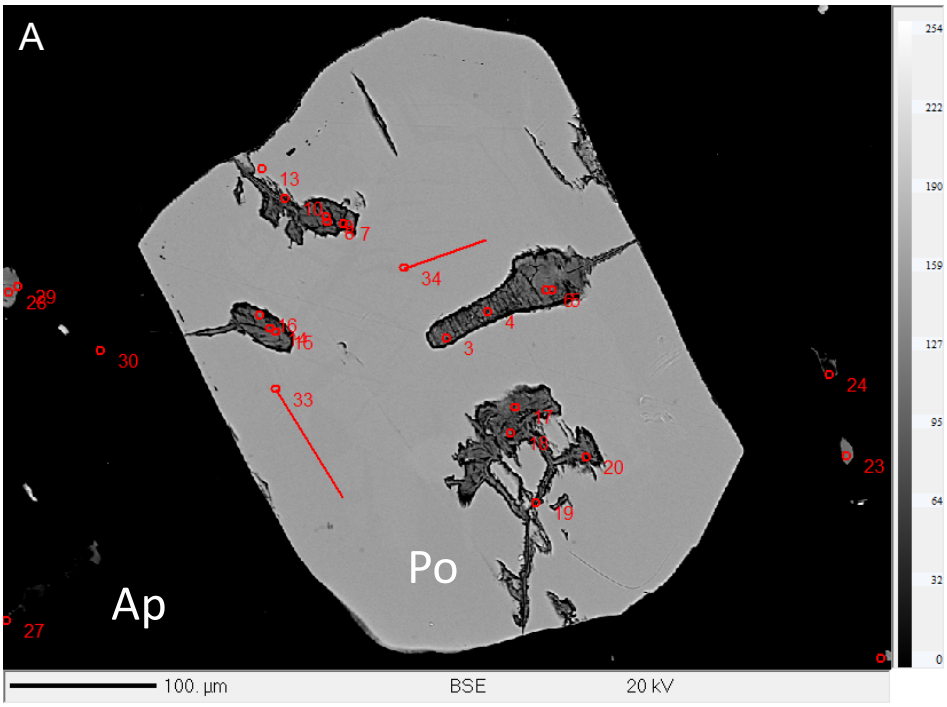

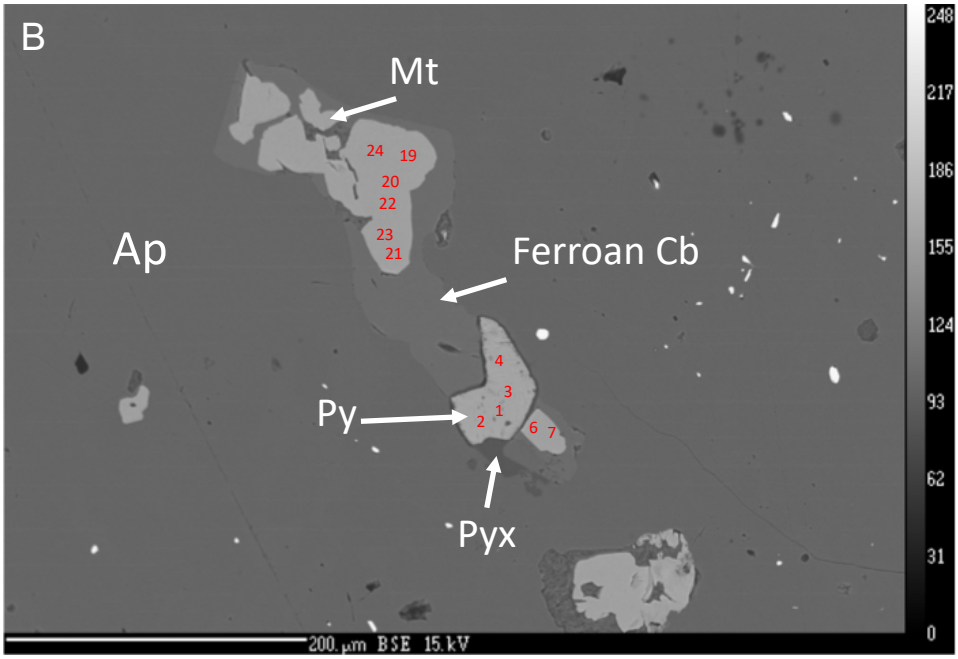

S3.

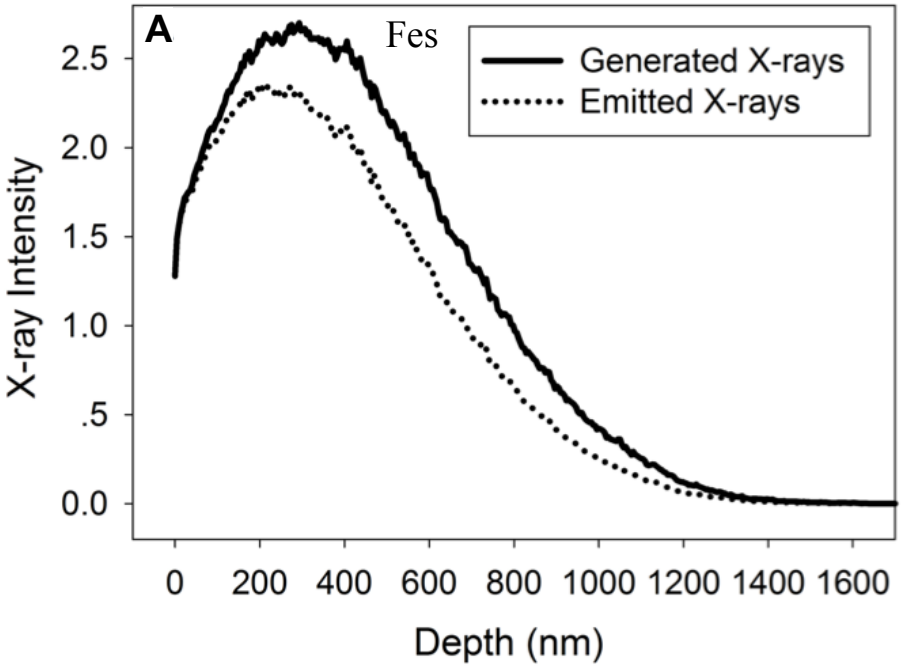
A
Fes
Generated X-rays
Emitted X-rays
X-ray Intensity
2.5
2.0
1.5
1.0
.5
0.0
0
200
400
600
800
1000
1200
1400
1600
Depth (nm)

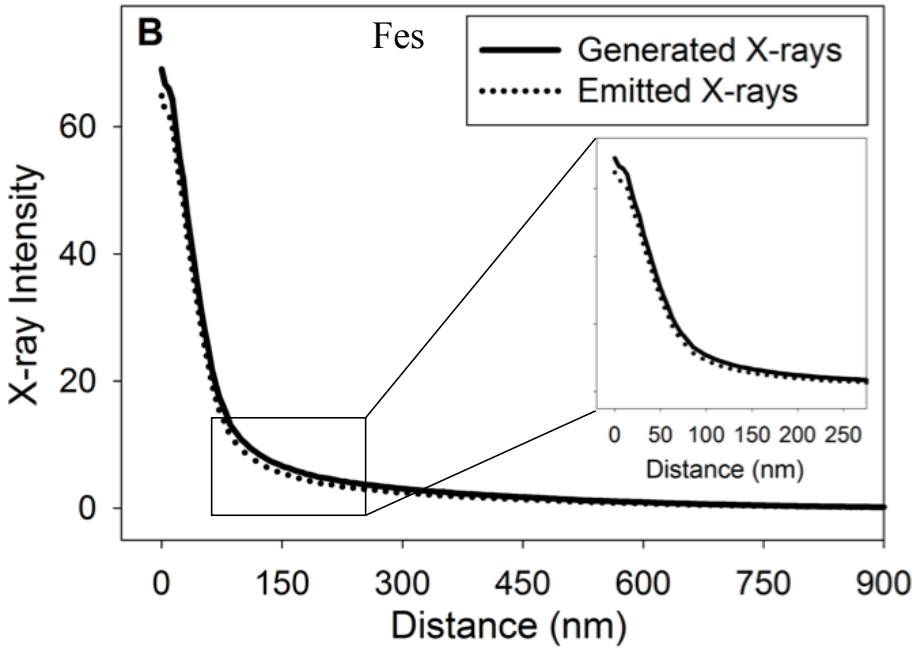
B
Fes
Generated X-rays
Emitted X-rays
X-ray Intensity
60
40
20
0
0
150
300
450
600
750
900
Distance (nm)
0
50
100
150
200
250
Distance (nm)

S4.

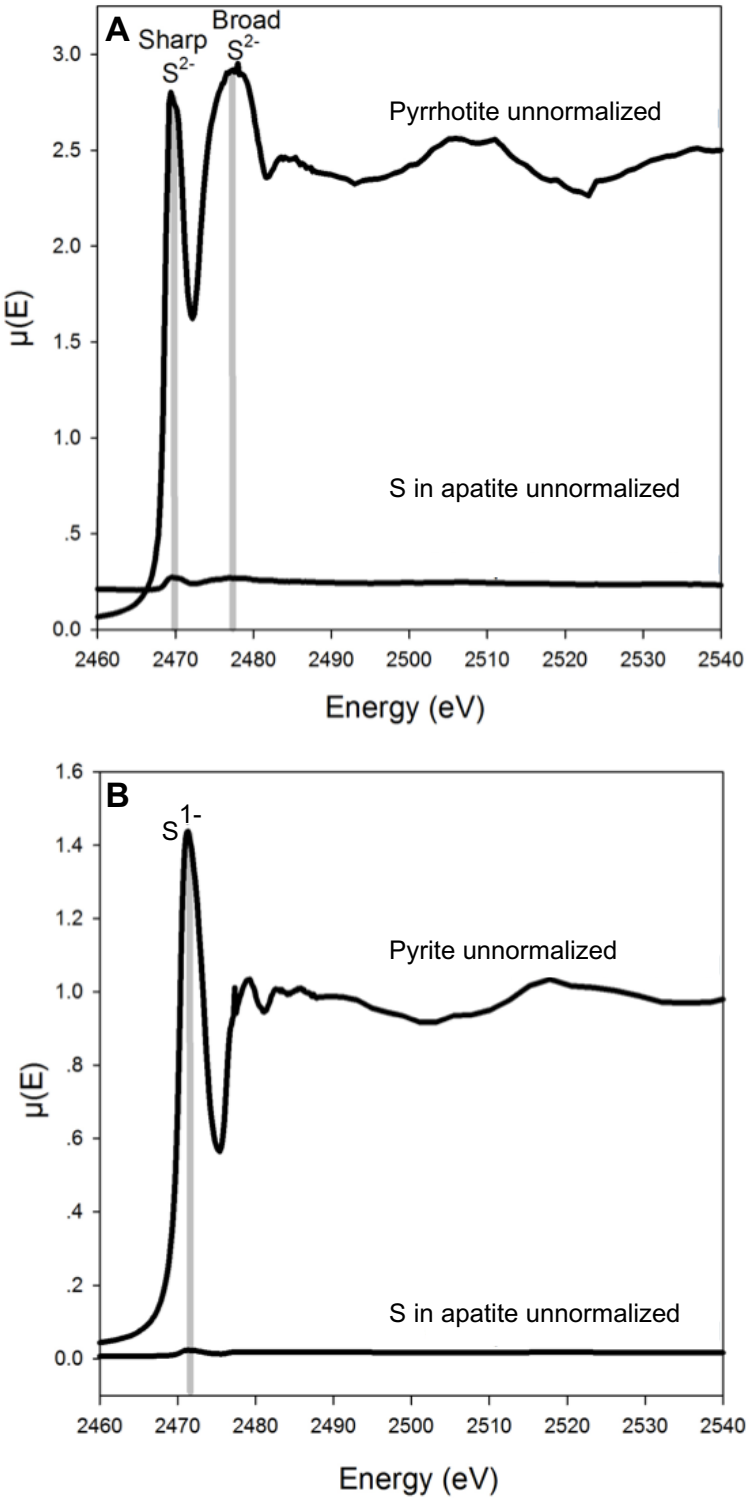
A
Sharp
S^{2-}
Broad
S^{2-}
Pyrrhotite unnormalized
S in apatite unnormalized
μ(E)
Energy (eV)
B
S^{1-}
Pyrite unnormalized
S in apatite unnormalized
μ(E)
Energy (eV)

S5.

Supplemental Data Table S1. Apatite A - EPMA Analyses
wt% oxide

Sample	AA2-1	AA2-2	AA2-3	AA2-4	AA2-5	AA2-6	AA2-7	AA2-8	AA2-9	AA2-10
F	2.21	2.55	2.43	2.35	2.33	2.40	2.51	2.26	2.31	2.23
Cl	0.79	0.58	0.55	0.56	0.51	0.59	0.56	0.52	0.52	0.59
Na2O	0.18	b.d.	b.d.	b.d.	0.08	b.d.	b.d.	b.d.	b.d.	b.d.
K2O	b.d.	b.d.	b.d.	b.d.	b.d.	b.d.	b.d.	b.d.	b.d.	b.d.
MgO	b.d.	b.d.	b.d.	b.d.	b.d.	b.d.	b.d.	b.d.	b.d.	b.d.
CaO	51.81	54.15	55.01	53.87	52.91	53.98	54.56	53.48	54.99	53.97
SiO2	0.21	0.20	0.25	0.23	1.62	0.13	0.23	0.26	0.16	0.20
P2O5**	40.91	42.31	41.79	42.56	41.10	42.34	41.85	42.71	42.20	41.87
TiO2	b.d.	b.d.	b.d.	b.d.	b.d.	b.d.	b.d.	b.d.	b.d.	b.d.
MnO	b.d.	b.d.	b.d.	b.d.	b.d.	b.d.	b.d.	b.d.	b.d.	b.d.
FeO	0.93	b.d.	b.d.	b.d.	0.07	b.d.	b.d.	0.11	b.d.	0.05
SrO	b.d.	b.d.	b.d.	b.d.	b.d.	b.d.	b.d.	b.d.	b.d.	b.d.
BaO	b.d.	b.d.	b.d.	b.d.	b.d.	b.d.	b.d.	b.d.	b.d.	b.d.
Al2O3	b.d.	b.d.	b.d.	b.d.	0.30	b.d.	b.d.	b.d.	0.01	b.d.
La2O3	0.13	b.d.	b.d.	0.20	b.d.	0.18	0.15	b.d.	b.d.	b.d.
Ce2O3	0.42	0.09	0.15	0.11	0.08	0.11	0.12	0.07	0.12	0.17
SO2	0.21	0.01	0.01	0.01	0.02	0.02	0.02	0.01	0.02	0.02
O = (F,Cl)	1.11	1.20	1.15	1.12	1.09	1.14	1.18	1.07	1.09	1.07
Total	97.38	99.36	99.87	99.70	98.88	99.41	99.55	99.37	100.18	99.02
OH wt% calc.	0.67	0.66	0.82	0.92	0.96	0.81	0.73	1.02	0.93	0.99
S (µg/g)	1038.2	68.9	57.6	30.6	97.3	88.1	84.9	41.9	77.2	99.5
Distance (µm)	0	73.8	147.59	221.39	295.18	368.98	442.78	516.57	590.37	664.16
F***	1.35	1.43	1.34	1.28	1.27	1.33	1.39	1.23	1.28	1.23
Cl***	0.26	0.18	0.16	0.16	0.15	0.18	0.17	0.15	0.16	0.17
OH***	0.39	0.4	0.49	0.56	0.58	0.49	0.44	0.62	0.56	0.6
F +Cl +OH	2.00	2.00	2.00	2.00	2.00	2.00	2.00	2.00	2.00	2.00

Sample	AA2-11	AA2-12	AA2-13	AA2-14	AA2-15	AA2-16	AA2-17	AA2-18	AA2-19	AA2-20
F	2.37	2.33	2.56	2.33	2.30	2.36	2.44	2.38	2.36	2.43
Cl	0.53	0.58	0.54	0.57	0.55	0.55	0.52	0.49	0.50	0.52
Na2O	b.d.	0.05	0.04	b.d.	0.04	b.d.	b.d.	b.d.	b.d.	0.04
K2O	b.d.	b.d.	b.d.	b.d.	b.d.	b.d.	b.d.	b.d.	b.d.	b.d.
MgO	b.d.	b.d.	b.d.	0.03	b.d.	b.d.	b.d.	b.d.	b.d.	b.d.
CaO	54.99	53.78	54.09	53.58	53.44	53.15	54.25	54.03	54.57	52.62
SiO2	0.15	0.51	0.25	0.26	0.16	0.13	0.16	0.08	0.06	0.19
P2O5**	42.19	42.43	41.57	42.21	41.96	42.45	42.74	42.34	41.44	41.72
TiO2	b.d.	b.d.	b.d.	b.d.	b.d.	0.02	b.d.	b.d.	b.d.	0.02
MnO	b.d.	b.d.	b.d.	b.d.	b.d.	b.d.	b.d.	b.d.	b.d.	b.d.
FeO	b.d.	b.d.	b.d.	b.d.	b.d.	b.d.	b.d.	b.d.	b.d.	b.d.
SrO	b.d.	b.d.	b.d.	b.d.	b.d.	b.d.	b.d.	b.d.	b.d.	b.d.
BaO	b.d.	b.d.	b.d.	b.d.	b.d.	b.d.	b.d.	b.d.	b.d.	b.d.
Al2O3	b.d.	b.d.	0.03	0.01	b.d.	b.d.	b.d.	b.d.	b.d.	b.d.
La2O3	b.d.	b.d.	b.d.	b.d.	b.d.	b.d.	b.d.	b.d.	b.d.	0.13
Ce2O3	0.13	0.14	0.22	0.17	0.18	0.11	0.09	0.13	0.10	0.11
SO2	0.00	0.01	0.02	0.01	0.01	0.02	0.02	0.02	0.02	0.03
O = (F,Cl)	1.12	1.11	1.20	1.11	1.09	1.12	1.15	1.11	1.10	1.14
Total	100.14	99.66	98.79	98.97	98.47	98.57	99.91	99.26	98.82	97.49
OH wt% calc.	0.89	0.93	0.69	0.91	0.92	0.89	0.83	0.90	0.88	0.83
S (µg/g)	23.4	50.7	80.5	71	73.1	106.9	90.5	82.8	85.1	139.6
Distance (µm)	737.96	811.76	885.55	959.35	1033.14	1106.94	1180.73	1254.53	1328.33	1402.12
F***	1.31	1.27	1.42	1.28	1.28	1.3	1.35	1.31	1.32	1.34
Cl***	0.16	0.17	0.16	0.17	0.16	0.16	0.15	0.14	0.15	0.15
OH***	0.54	0.56	0.42	0.55	0.56	0.54	0.5	0.55	0.53	0.5
F +Cl +OH	2.00	2.00	2.00	2.00	2.00	2.00	2.00	2.00	2.00	2.00

Sample	AA2-21	AA2-22	AA2-23	AA2-24	AA2-25	AA2-26	AA2-27	AA2-28	AA2-29	AA2-30
F	2.61	2.40	2.57	2.59	2.37	2.29	2.55	2.55	2.32	2.14
Cl	0.53	0.51	0.53	0.50	0.46	0.46	0.46	0.50	0.52	0.71
Na2O	0.04	b.d.	b.d.	b.d.	b.d.	b.d.	b.d.	b.d.	b.d.	b.d.
K2O	b.d.	b.d.	b.d.	b.d.	b.d.	b.d.	b.d.	b.d.	b.d.	b.d.
MgO	b.d.	b.d.	b.d.	b.d.	0.02	b.d.	b.d.	b.d.	b.d.	b.d.
CaO	54.00	53.70	54.28	53.36	53.65	53.63	54.71	53.02	54.61	53.01
SiO2	0.26	0.19	0.27	0.30	0.09	b.d.	0.33	0.30	0.25	0.53
P2O5**	41.80	42.04	41.63	41.09	43.30	42.63	41.95	41.89	42.55	41.53
TiO2	b.d.	b.d.	0.02	b.d.	b.d.	b.d.	b.d.	b.d.	b.d.	b.d.
MnO	b.d.	b.d.	0.06	b.d.	b.d.	b.d.	b.d.	b.d.	b.d.	b.d.
FeO	b.d.	b.d.	b.d.	0.19	b.d.	0.11	b.d.	b.d.	b.d.	b.d.
SrO	b.d.	b.d.	b.d.	b.d.	b.d.	b.d.	b.d.	b.d.	b.d.	b.d.
BaO	b.d.	b.d.	b.d.	b.d.	b.d.	b.d.	b.d.	b.d.	b.d.	b.d.
Al2O3	b.d.	0.01	0.01	b.d.	0.01	b.d.	b.d.	0.01	b.d.	b.d.
La2O3	0.21	b.d.	b.d.	b.d.	b.d.	b.d.	b.d.	b.d.	b.d.	0.16
Ce2O3	0.33	b.d.	0.07	0.09	b.d.	0.08	0.08	0.06	b.d.	0.41
SO2	0.07	0.01	0.02	0.11	0.01	0.01	0.01	0.01	0.02	0.19
O = (F,Cl)	1.22	1.13	1.20	1.21	1.10	1.07	1.18	1.18	1.09	1.06
Total	99.27	98.60	98.94	97.70	99.76	99.14	99.67	97.91	100.11	98.62
OH wt% calc.	0.63	0.86	0.68	0.67	0.95	1.00	0.75	0.75	0.94	1.01
S (µg/g)	344	30.1	102	553.5	67.5	41.5	46.6	56.4	82.2	928
Distance (µm)	1475.92	1549.72	1623.51	1697.31	1771.1	1844.9	1918.69	1992.49	2066.29	2140.08
F***	1.46	1.33	1.43	1.44	1.29	1.26	1.41	1.4	1.28	1.18
Cl***	0.16	0.15	0.16	0.15	0.13	0.14	0.14	0.15	0.15	0.21
OH***	0.38	0.52	0.41	0.41	0.57	0.6	0.45	0.45	0.57	0.62
F +Cl +OH	2.00	2.00	2.00	2.00	2.00	2.00	2.00	2.00	2.00	2.00

Sample	AA2-31	AA2-32	AA2-33	AA2-34	AA2-35	AA2-36	AA2-38	AA2-39	AA2-40
F	2.23	2.31	2.19	2.47	2.33	2.41	2.31	2.34	2.38
Cl	0.53	0.50	0.49	0.48	0.65	0.57	0.48	0.50	0.51
Na2O	b.d.	b.d.	b.d.	b.d.	b.d.	b.d.	b.d.	b.d.	b.d.
K2O	b.d.	b.d.	b.d.	b.d.	b.d.	b.d.	b.d.	b.d.	b.d.
MgO	b.d.	b.d.	b.d.	b.d.	0.03	b.d.	b.d.	b.d.	b.d.
CaO	54.03	53.86	54.63	53.28	53.67	52.69	52.73	53.90	52.91
SiO2	0.14	0.14	0.11	0.29	0.17	0.54	0.15	0.22	0.29
P2O5**	42.21	41.67	42.52	41.78	42.02	41.78	42.29	41.45	41.58
TiO2	b.d.	b.d.	b.d.	b.d.	b.d.	b.d.	0.02	b.d.	b.d.
MnO	b.d.	b.d.	b.d.	b.d.	b.d.	b.d.	b.d.	b.d.	b.d.
FeO	b.d.	b.d.	b.d.	b.d.	b.d.	b.d.	b.d.	b.d.	0.09
SrO	b.d.	b.d.	b.d.	b.d.	b.d.	b.d.	b.d.	b.d.	b.d.
BaO	b.d.	b.d.	b.d.	b.d.	b.d.	b.d.	b.d.	b.d.	b.d.
Al2O3	0.02	b.d.	b.d.	0.01	b.d.	b.d.	b.d.	b.d.	b.d.
La2O3	b.d.	b.d.	b.d.	b.d.	b.d.	b.d.	b.d.	b.d.	0.20
Ce2O3	0.15	0.07	0.09	b.d.	0.11	0.13	0.10	0.12	0.10
SO2	0.01	0.01	0.01	0.01	0.09	0.01	0.01	0.01	0.01
O = (F,Cl)	1.06	1.09	1.05	1.15	1.13	1.14	1.08	1.10	1.12
Total	99.24	98.40	100.04	97.99	98.79	97.81	97.81	98.32	97.83
OH wt% calc.	1.00	0.93	1.04	0.82	0.85	0.82	0.80	0.88	0.87
S (µg/g)	53.4	56.8	66	71	441.9	71.1	65.5	68.5	52.1
Distance (µm)	2213.88	2287.67	2361.47	2435.27	2509.06	2582.86	2730.45	2804.24	2878.04
F***	1.24	1.28	1.2	1.36	1.29	1.33	1.38	1.32	1.32
Cl***	0.16	0.15	0.17	0.14	0.19	0.17	0.15	0.15	0.15
OH***	0.6	0.57	0.63	0.5	0.51	0.5	0.47	0.53	0.52
F +Cl +OH	2.00	2.00	2.00	2.00	2.00	2.00	2.00	2.00	2.00

Sample	AA2-41	AA2-42	AA2-43	AA2-44	AA2-45	AA2-46	AA2-47	AA2-48	AA2-49	AA2-50	SD wt% oxide	Det limit (µg/g)
F	2.42	2.50	2.57	2.51	2.31	2.28	2.48	2.48	2.33	2.40	0.26*	2344
Cl	0.46	0.56	0.45	0.42	0.63	0.47	0.51	0.46	0.44	0.60	0.04*	188
Na2O	b.d.	b.d.	b.d.	b.d.	b.d.	b.d.	b.d.	b.d.	b.d.	b.d.	0.04	440
K2O	b.d.	b.d.	b.d.	b.d.	b.d.	b.d.	b.d.	b.d.	b.d.	b.d.	b.d.	488
MgO	b.d.	b.d.	b.d.	b.d.	b.d.	b.d.	b.d.	b.d.	b.d.	b.d.	0.01	279
CaO	54.36	54.15	53.90	53.98	53.42	53.83	54.80	53.36	54.40	53.66	1.71	713
SiO2	0.80	0.14	0.25	0.07	0.35	0.38	0.12	0.08	0.44	0.04	0.08	366
P2O5**	41.10	41.96	42.05	42.70	40.93	41.73	42.18	42.22	42.01	42.43	0.67	1311
TiO2	b.d.	b.d.	b.d.	b.d.	b.d.	b.d.	b.d.	b.d.	b.d.	b.d.	0.01	282
MnO	b.d.	b.d.	b.d.	b.d.	b.d.	b.d.	b.d.	b.d.	b.d.	b.d.	0.04	740
FeO	b.d.	b.d.	b.d.	b.d.	b.d.	b.d.	b.d.	b.d.	b.d.	b.d.	0.06	716
SrO	b.d.	b.d.	b.d.	b.d.	b.d.	b.d.	b.d.	b.d.	b.d.	b.d.	0.06	1588
BaO	b.d.	b.d.	b.d.	b.d.	b.d.	b.d.	b.d.	b.d.	b.d.	b.d.	0.10	1812
Al2O3	0.01	0.01	b.d.	b.d.	0.01	b.d.	b.d.	b.d.	b.d.	b.d.	0.02	236
La2O3	b.d.	b.d.	b.d.	b.d.	0.16	b.d.	b.d.	b.d.	b.d.	b.d.	b.d.	1809
Ce2O3	0.16	0.09	0.08	0.11	0.36	0.07	0.06	0.08	0.10	0.19	0.09	894
SO2	0.01	0.01	0.02	0.01	0.13	0.01	0.01	0.03	0.01	0.02	0.01	69
O = (F,Cl)	1.12	1.18	1.18	1.15	1.11	1.07	1.16	1.15	1.08	1.14		
Total	99.05	99.00	98.87	99.49	98.04	98.67	99.80	98.41	99.61	99.02		
OH wt% calc.	0.84	0.75	0.74	0.83	0.86	0.98	0.79	0.84	0.96	0.84		
S (µg/g)	74.9	61.8	85.6	72.6	644.2	33.3	38.1	132.6	53.9	77.1		
Distance (µm)	2951.84	3025.63	3099.43	3173.23	3247.02	3320.82	3394.61	3468.41	3542.2	3616		
F***	1.35	1.38	1.42	1.38	1.29	1.27	1.37	1.36	1.29	1.32		
Cl***	0.14	0.17	0.13	0.12	0.19	0.14	0.15	0.13	0.13	0.18		
OH***	0.51	0.45	0.45	0.5	0.52	0.59	0.47	0.51	0.58	0.51		
F +Cl +OH	2.00	2.00	2.00	2.00	2.00	2.00	2.00	2.00	2.00	2.00		

Notes:
n = 49. Analyses given in 1σ
standard error of mean

b.d. is bellow detection limit
Calculated as OH assuming the halogen site is filled with F + Cl + OH. O=F,Cl is correction factor
*SD wt% averages are presented for each oxide. Average SD for F and Cl represented in wt%.
** P2O5 drift was detected and corrected based on systematic shift in both unknown and durango apatite measurment
***Anion Ratio for Ternary Plot

Apatite B - EPMA Analyses
wt% oxide

Sample	AB1-1	AB1-2	AB1-3	AB1-4	AB1-5	AB1-6	AB1-7	AB1-8	AB1-9	AB1-10	AB1-11	AB1-12	AB1-13	SD Wt% Oxide	Det limit (µg/g)
F	2.47	2.39	2.24	2.50	2.52	2.36	2.23	2.47	2.32	2.06	2.32	2.81	2.33	0.27*	2344
Cl	0.32	0.36	0.40	0.46	0.48	0.52	0.53	0.43	0.49	0.63	0.52	0.43	0.48	0.028*	188
Na2O	0.05	b.d.	b.d.	0.12	0.03	b.d.	b.d.	0.04	b.d.	0.18	0.16	b.d.	b.d.	0.0517	440
MgO	b.d.	0.02	b.d.	b.d.	b.d.	b.d.	b.d.	b.d.	b.d.	b.d.	b.d.	b.d.	b.d.	0.02	279
Al2O3	b.d.	b.d.	b.d.	b.d.	0.02	b.d.	0.02	b.d.	b.d.	b.d.	b.d.	b.d.	b.d.	0.02	236
SiO2	0.58	0.43	0.67	0.14	0.44	0.42	0.67	0.16	0.49	2.23	0.23	0.89	0.36	0.10	366
P2O5**	42.23	41.86	41.52	42.26	42.26	41.58	42.08	42.12	41.78	40.62	41.89	40.06	41.24	1.16	1311
CaO	54.77	54.28	54.21	53.25	54.64	53.94	54.13	54.15	53.76	52.90	54.36	52.38	54.38	1.52	713
K2O	b.d.	b.d.	b.d.	b.d.	b.d.	b.d.	b.d.	b.d.	b.d.	b.d.	b.d.	b.d.	b.d.	0.03	488
TiO2	b.d.	b.d.	b.d.	b.d.	b.d.	b.d.	b.d.	0.02	b.d.	0.02	b.d.	b.d.	b.d.	0.03	282
SO3	0.02	0.01	0.01	0.12	0.02	0.05	0.02	0.01	0.01	0.20	0.20	0.01	0.01	0.01	69
MnO	b.d.	b.d.	b.d.	b.d.	b.d.	b.d.	b.d.	b.d.	b.d.	b.d.	b.d.	b.d.	b.d.	0.02	740
FeO	0.10	b.d.	b.d.	0.09	b.d.	b.d.	b.d.	b.d.	0.10	b.d.	0.09	0.06	b.d.	0.07	716
SrO	b.d.	b.d.	b.d.	b.d.	b.d.	b.d.	b.d.	b.d.	b.d.	b.d.	b.d.	b.d.	b.d.	0.09	1588
BaO	b.d.	b.d.	b.d.	b.d.	b.d.	b.d.	b.d.	b.d.	b.d.	b.d.	b.d.	b.d.	b.d.	0.03	1812
La2O3	b.d.	b.d.	b.d.	b.d.	b.d.	b.d.	b.d.	b.d.	b.d.	b.d.	b.d.	b.d.	b.d.	b.d.	1809
Ce2O3	0.21	0.09	0.13	0.23	0.13	0.11	b.d.	0.09	0.13	0.32	0.25	0.09	0.14	0.10	894
O = (F,Cl)	1.11	1.09	1.03	1.16	1.17	1.11	1.06	1.14	1.09	1.01	1.09	1.28	1.09		
OH wt% calc.	0.93	0.95	1.06	0.80	0.80	0.89	1.03	0.84	0.94	1.13	0.95	0.44	0.92		
Total	100.58	99.30	99.20	98.81	100.18	98.76	99.66	99.21	98.93	99.30	99.87	95.90	98.77		
S (µg/g)	79.5	31.8	57.7	473.7	90.5	214.4	87.6	55.6	35.8	812	812.8	36.5	31.1		
Distance (µm)	0	196.92	393.83	590.75	787.67	984.58	1181.5	1378.42	1575.33	1772.25	1969.17	2166.08	2363		
F***	1.34	1.32	1.24	1.38	1.37	1.31	1.22	1.36	1.28	1.13	1.27	1.60	1.29		
Cl***	0.09	0.11	0.12	0.14	0.14	0.15	0.16	0.13	0.14	0.19	0.15	0.13	0.14		
OH***	0.56	0.57	0.64	0.48	0.49	0.54	0.62	0.51	0.57	0.68	0.57	0.27	0.56		
F +Cl +OH	2.00	2.00	2.00	2.00	2.00	2.00	2.00	2.00	2.00	2.00	2.00	2.00	2.00		

Notes:
b.d. is bellow detection limit
Calculated as OH assuming the halogen site is filled with F + Cl + OH. O=F,Cl is correction factor
*SD Wt% averages are presented for each oxide. SD for F and Cl represented in Wt%.
** P2O5 drift was detected and corrected based on systematic shift in both unknown and durango apatite measurment
***Anion Ratio for Ternary Plot

Supplementary Data Table S2. Pyrite, Pyrrhotite, Magnetite - EPMA Analyses
wt%

	Fig. S3 A														
Sample	**PO5-3**	**PO5-4**	**PO5-5**	**PO5-6**	**PO5-7**	**PO5-8**	**PO5-9**	**PO5-10**	**PO5-13**	**PO5-14**	**PO5-16**	**PO5-23**	**PO5-33-1**	**PO5-33-2**	**PO5-33-3**
S	50.2594	49.8577	47.3146	50.4215	48.9397	46.6415	42.9442	49.0948	42.3523	51.2194	47.689	53.088	39.4545	39.7309	39.3944
Fe	43.6569	44.1129	43.5742	42.3834	42.954	43.4841	33.0615	43.2995	50.8238	42.2024	43.9595	44.8693	58.7683	58.9106	58.6422
Ni	1.2469	1.2263	1.1981	1.2776	1.3017	0.824	16.4432	1.1307	0.5722	1.1468	0.8756	0.8432	0.3609	0.3599	0.3388
O	3.6273	3.6426	7.0948	5.0612	5.6642	7.0259	4.5038	4.1451	5.3466	2.9345	2.3694	0.2931	0.3198	0.3409	0.3032
Total	98.7905	98.8394	99.1817	99.1437	98.8596	97.9754	96.9526	97.67	99.0949	97.503	94.8934	99.0936	98.9035	99.3422	98.6786
S (µg/g)	502594	498577	473146	504215	489397	466415	429442	490948	423523	512194	476890	530880	394545	397309	393944
Distance (µm)													0	21.44	42.88
Description	Fe-O-Ni-S phase	Fe-O-Ni-S phase	Fe-O-Ni-S phase	Fe-O-Ni-S phase	Fe-O-Ni-S phase	Fe-O-Ni-S phase	Fe-O-Ni-S phase	Fe-O-Ni-S phase	Fe-O-Ni-S phase	Fe-O-Ni-S phase	Fe-O-Ni-S phase	Pyrite	Pyrrhotite	Pyrrhotite	Pyrrhotite

							Fig. S3B			
Sample	**PO5-33-4**	**PO5-33-5**	**PO5-34-1**	**PO5-34-2**	**PO5-34-3**	**PO5-34-4**	**PO5-34-5**	**PY4-1**	**PY4-2**	**PY4-3**
S	39.6651	39.5321	39.2635	38.9436	38.8724	38.6618	38.8667	55.5591	53.7168	53.4169
Fe	59.2181	59.1523	58.8677	58.7391	59.2631	58.7469	58.9885	45.846	45.9718	45.7597
Ni	0.2776	0.2138	0.5993	0.7854	0.7925	0.7847	0.7864	b.d.	b.d.	b.d.
O	0.3014	0.3163	0.3423	0.3357	0.2869	0.28	0.2382	0.3184	0.2139	0.2105
Total	99.4622	99.2145	99.0727	98.8038	99.2148	98.4734	98.8798	101.7344	99.9189	99.4041
S (µg/g)	396651	395321	392635	389436	388724	386618	388667	555591	537168	534169
Distance (µm)	64.32	85.76	0	14.55	29.09	43.64	58.19			
Description	Pyrrhotite	Pyrrhotite	Pyrrhotite	Pyrrhotite	Pyrrhotite	Pyrrhotite	Pyrrhotite	Pyrite	Pyrite	Pyrite

Sample	PY4-4	PY4-6	PY4-7	PY4-19	PY4-20	PY4-21	PY4-22	PY4-23	PY4-24	SD wt%	Det Limit (µg/g)
S	51.6846	0.031	0.0283	b.d	b.d	b.d	b.d	b.d	b.d	0.177	101
Fe	45.6394	70.4397	70.5804	71.0204	71.2419	71.2294	71.0781	71.2369	70.6933	0.3	254
Ni	b.d.	b.d.	b.d.	b.d.	b.d.	b.d.	b.d.	b.d.	b.d.	0.0159	166
O	0.2431	25.9687	26.0101	27.2101	27.0558	27.1371	26.726	27.3265	26.8616	0.196	965
Total	97.572	96.4404	96.6182	98.2342	98.3052	98.3721	97.8113	98.5779	97.5506		
S (µg/g)	516846	310	283	b.d.	b.d.	b.d.	b.d.	b.d.	b.d.		
Distance (µm)											
Description	Pyrite	Magnetite	Magnetite	Magnetite	Magnetite	Magnetite	Magnetite	Magnetite	Magnetite		

Notes:
Oxygen was measured directly on FEOX, FEOX = Fe : 69.9426%, O : 30.0574%
n= 34. Analyses given in 1σ
standard error of mean

b.d. is bellow detection limit

Supplementary Data Table S3. Pyroxene & Ferroan Carbonate-EPMA Analyses
wt% oxide - Pyroxene

Sample	PY-72-1	PY-73-2	Det limit (µg/g):	SD wt% oxide:
MgO	20.08	19.28	65.00	0.29
Al2O3	0.08	0.44	53.00	0.02
SiO2	55.46	55.68	81.00	0.41
TiO2	b.d	b.d	84.00	0.01
CaO	13.01	12.97	73.00	0.14
P2O5	0.41	0.46	66.00	0.02
V2O3	b.d.	b.d.	63.00	0.01
Cr2O3	b.d	b.d	64.00	0.01
FeO	9.71	9.89	73.00	0.10
MnO	0.08	0.12	236.00	0.03
Total	98.84	98.85		

Notes:
n = 2
b.d. is bellow detection limit

wt% oxide-Ferroan Carbonate

Sample	FC-1	FC- 6	FC - 7	FC - 8	FC - 9	Det limit (µg/g):	SD wt% oxide
MgO	0.46	0.35	b.d.	0.03	0.53	256.00	0.04
CaO	5.97	3.33	0.11	0.33	4.90	392.00	0.55
MnO	0.96	0.43	b.d.	b.d	0.75	402.00	0.05
FeO	53.50	65.83	63.04	62.78	58.92	471.00	0.41
CO2	39.12	30.05	36.83	36.85	34.90		
Total	100.00	100.00	100.00	99.97	100.00		

Notes:
n=5
b.d. is bellow detection limit
Carbonate data was matrix corrected for presence of Carbon.

Supplementary Data Table S4. EPMA Transects 1-9

wt% oxide

	Sample	SO2	S (µg/g)	Cl	P2O5	CaO	MnO	FeO	TiO2	La2O3	Na2O	Al2O3	SiO2	F	Ce2O3	Total	Distance (µm)	Sulfur Det limit (µg/g)
Apatite A:	**Pyrrhotite**																0	
	Pyrrhotite																5.66	
	Pyrrhotite																11.31	
	AA-Trans1-1	0.1591	796	0.48	40.4205	53.7293	0.0258	0.7462	0.0167	0.2463	0.0539	0.3212	0.8985	2.38	0.5388	100.0163	16.97	30
	AA-Trans1-2	0.113	565	0.48	40.4205	53.7293	0.0258	0.7462	0.0167	0.2463	0.0539	0.3212	0.8985	2.38	0.5388	99.9702	22.63	30
	AA-Trans1-3	0.0536	268	0.48	40.4205	53.7293	0.0258	0.7462	0.0167	0.2463	0.0539	0.3212	0.8985	2.38	0.5388	99.9108	28.29	30
	AA-Trans1-4	0.0193	97	0.48	40.4205	53.7293	0.0258	0.7462	0.0167	0.2463	0.0539	0.3212	0.8985	2.38	0.5388	99.8765	33.94	31
	AA-Trans1-5	0.0144	72	0.48	40.4205	53.7293	0.0258	0.7462	0.0167	0.2463	0.0539	0.3212	0.8985	2.38	0.5388	99.8716	39.6	30
	AA-Trans1-6	0.0306	153	0.48	40.4205	53.7293	0.0258	0.7462	0.0167	0.2463	0.0539	0.3212	0.8985	2.38	0.5388	99.8878	45.26	30
	AA-Trans1-7	0.0714	358	0.48	40.4205	53.7293	0.0258	0.7462	0.0167	0.2463	0.0539	0.3212	0.8985	2.38	0.5388	99.9286	50.92	30
	AA-Trans1-8	0.07	350	0.48	40.4205	53.7293	0.0258	0.7462	0.0167	0.2463	0.0539	0.3212	0.8985	2.38	0.5388	99.9272	56.57	30
	AA-Trans1-9	0.0688	344	0.48	40.4205	53.7293	0.0258	0.7462	0.0167	0.2463	0.0539	0.3212	0.8985	2.38	0.5388	99.926	62.23	30
	AA-Trans1-10	0.0651	326	0.48	40.4205	53.7293	0.0258	0.7462	0.0167	0.2463	0.0539	0.3212	0.8985	2.38	0.5388	99.9223	67.89	30
	AA-Trans1-11	0.0696	348	0.48	40.4205	53.7293	0.0258	0.7462	0.0167	0.2463	0.0539	0.3212	0.8985	2.38	0.5388	99.9268	73.55	31
	AA-Trans1-12	0.0655	328	0.48	40.4205	53.7293	0.0258	0.7462	0.0167	0.2463	0.0539	0.3212	0.8985	2.38	0.5388	99.9227	79.2	31
Apatite B:	**Pyrite**																0	
	AB-Trans6-1	0.098	491	0.48	40.4205	53.7293	0.0258	0.7462	0.0167	0.2463	0.0539	0.3212	0.8985	2.38	0.5388	99.9552	10.22	30
	AB-Trans6-2	0.0345	173	0.48	40.4205	53.7293	0.0258	0.7462	0.0167	0.2463	0.0539	0.3212	0.8985	2.38	0.5388	99.8917	20.45	31
	AB-Trans6-3	0.0201	101	0.48	40.4205	53.7293	0.0258	0.7462	0.0167	0.2463	0.0539	0.3212	0.8985	2.38	0.5388	99.8773	30.67	30
	AB-Trans6-4	0.0214	107	0.48	40.4205	53.7293	0.0258	0.7462	0.0167	0.2463	0.0539	0.3212	0.8985	2.38	0.5388	99.8786	40.89	30
	AB-Trans6-5	0.015	75	0.48	40.4205	53.7293	0.0258	0.7462	0.0167	0.2463	0.0539	0.3212	0.8985	2.38	0.5388	99.8722	51.11	30
	AB-Trans6-6	0.0111	55	0.48	40.4205	53.7293	0.0258	0.7462	0.0167	0.2463	0.0539	0.3212	0.8985	2.38	0.5388	99.8683	61.33	31
	AB-Trans6-7	0.0114	57	0.48	40.4205	53.7293	0.0258	0.7462	0.0167	0.2463	0.0539	0.3212	0.8985	2.38	0.5388	99.8686	71.55	31
	AB-Trans6-8	0.0128	64	0.48	40.4205	53.7293	0.0258	0.7462	0.0167	0.2463	0.0539	0.3212	0.8985	2.38	0.5388	99.87	81.78	30
	AB-Trans6-9	0.0112	56	0.48	40.4205	53.7293	0.0258	0.7462	0.0167	0.2463	0.0539	0.3212	0.8985	2.38	0.5388	99.8684	92	31
Apatite B:	**Pyrite**																0	
	AB-Trans7-1	0.1163	582	0.48	40.4205	53.7293	0.0258	0.7462	0.0167	0.2463	0.0539	0.3212	0.8985	2.38	0.5388	99.9735	11.55	33
	AB-Trans7-2	0.0374	187	0.48	40.4205	53.7293	0.0258	0.7462	0.0167	0.2463	0.0539	0.3212	0.8985	2.38	0.5388	99.8946	23.11	33
	AB-Trans7-3	0.0164	82	0.48	40.4205	53.7293	0.0258	0.7462	0.0167	0.2463	0.0539	0.3212	0.8985	2.38	0.5388	99.8736	34.67	32
	AB-Trans7-4	0.0221	110	0.48	40.4205	53.7293	0.0258	0.7462	0.0167	0.2463	0.0539	0.3212	0.8985	2.38	0.5388	99.8793	46.22	30
	AB-Trans7-5	0.0197	99	0.48	40.4205	53.7293	0.0258	0.7462	0.0167	0.2463	0.0539	0.3212	0.8985	2.38	0.5388	99.8769	57.78	30
	AB-Trans7-6	0.0313	157	0.48	40.4205	53.7293	0.0258	0.7462	0.0167	0.2463	0.0539	0.3212	0.8985	2.38	0.5388	99.8885	69.33	30
	AB-Trans7-7	0.1685	843	0.48	40.4205	53.7293	0.0258	0.7462	0.0167	0.2463	0.0539	0.3212	0.8985	2.38	0.5388	100.0257	80.89	30
	AB-Trans7-8	0.1701	851	0.48	40.4205	53.7293	0.0258	0.7462	0.0167	0.2463	0.0539	0.3212	0.8985	2.38	0.5388	100.0273	92.45	30
	AB-Trans7-9	0.1763	883	0.48	40.4205	53.7293	0.0258	0.7462	0.0167	0.2463	0.0539	0.3212	0.8985	2.38	0.5388	100.0335	104	31
Apatite B:	**Carbonate**																0	
	AB-Trans8-2	b.d.	18	0.48	40.4205	53.7293	0.0258	0.7462	0.0167	0.2463	0.0539	0.3212	0.8985	2.38	0.5388	99.8607	11.33	32
	AB-Trans8-3	0.0187	94	0.48	40.4205	53.7293	0.0258	0.7462	0.0167	0.2463	0.0539	0.3212	0.8985	2.38	0.5388	99.8759	22.67	30
	AB-Trans8-4	0.0232	116	0.48	40.4205	53.7293	0.0258	0.7462	0.0167	0.2463	0.0539	0.3212	0.8985	2.38	0.5388	99.8804	34	30
	AB-Trans8-5	0.0113	57	0.48	40.4205	53.7293	0.0258	0.7462	0.0167	0.2463	0.0539	0.3212	0.8985	2.38	0.5388	99.8685	45.33	29
	AB-Trans8-6	0.0048	24	0.48	40.4205	53.7293	0.0258	0.7462	0.0167	0.2463	0.0539	0.3212	0.8985	2.38	0.5388	99.862	56.67	30
	AB-Trans8-7	0.0136	68	0.48	40.4205	53.7293	0.0258	0.7462	0.0167	0.2463	0.0539	0.3212	0.8985	2.38	0.5388	99.8708	68	30
	AB-Trans8-8	0.0121	61	0.48	40.4205	53.7293	0.0258	0.7462	0.0167	0.2463	0.0539	0.3212	0.8985	2.38	0.5388	99.8693	79.33	31
	AB-Trans8-9	0.0123	61	0.48	40.4205	53.7293	0.0258	0.7462	0.0167	0.2463	0.0539	0.3212	0.8985	2.38	0.5388	99.8695	90.67	30
	AB-Trans8-10	0.0172	86	0.48	40.4205	53.7293	0.0258	0.7462	0.0167	0.2463	0.0539	0.3212	0.8985	2.38	0.5388	99.8744	102	30
Apatite B:	**Carbonate**																0	
	AB-Trans9-2	b.d.	b.d	0.48	40.4205	53.7293	0.0258	0.7462	0.0167	0.2463	0.0539	0.3212	0.8985	2.38	0.5388	99.857	10.89	33
	AB-Trans9-3	b.d.	b.d.	0.48	40.4205	53.7293	0.0258	0.7462	0.0167	0.2463	0.0539	0.3212	0.8985	2.38	0.5388	99.8605	21.78	32
	AB-Trans9-4	0.1205	603	0.48	40.4205	53.7293	0.0258	0.7462	0.0167	0.2463	0.0539	0.3212	0.8985	2.38	0.5388	99.9777	32.67	31
	AB-Trans9-5	0.1778	890	0.48	40.4205	53.7293	0.0258	0.7462	0.0167	0.2463	0.0539	0.3212	0.8985	2.38	0.5388	100.035	43.55	30
	AB-Trans9-6	0.1764	883	0.48	40.4205	53.7293	0.0258	0.7462	0.0167	0.2463	0.0539	0.3212	0.8985	2.38	0.5388	100.0336	54.45	30
	AB-Trans9-7	0.0681	341	0.48	40.4205	53.7293	0.0258	0.7462	0.0167	0.2463	0.0539	0.3212	0.8985	2.38	0.5388	99.9253	65.33	30
	AB-Trans9-8	0.0203	101	0.48	40.4205	53.7293	0.0258	0.7462	0.0167	0.2463	0.0539	0.3212	0.8985	2.38	0.5388	99.8775	76.22	30
	AB-Trans9-9	0.0221	110	0.48	40.4205	53.7293	0.0258	0.7462	0.0167	0.2463	0.0539	0.3212	0.8985	2.38	0.5388	99.8793	87.11	30
	AB-Trans9-10	0.0222	111	0.48	40.4205	53.7293	0.0258	0.7462	0.0167	0.2463	0.0539	0.3212	0.8985	2.38	0.5388	99.8794	98	31

Notes:

Trace sulfur was Stoichiometrically matrix corrected with apatite.

Sulfur SD wt% oxide: 0.03%

Transects 2-5 Apatite A:

wt% oxide

	Transect 2									
Sample	Pyrrhotite	AA-Trans2-2	AA-Trans2-3	AA-Trans2-4	AA-Trans2-5	AA-Trans2-6	AA-Trans2-7	AA-Trans2-8	AA-Trans2-9	AA-Trans2-10
Cl		0.41	0.35	0.32	0.33	0.30	0.32	0.33	0.33	0.35
P2O5		41.72	42.40	42.53	41.90	41.95	42.12	42.22	42.30	41.30
CaO		55.16	55.60	54.86	54.89	55.47	55.05	55.38	55.57	54.72
MnO		b.d.	b.d.	b.d.	b.d.	b.d.	b.d.	b.d.	b.d.	b.d.
FeO		0.61	0.29	0.17	0.09	0.10	b.d.	b.d.	b.d.	b.d.
TiO2		b.d.	b.d.	b.d.	b.d.	b.d.	b.d.	b.d.	b.d.	b.d.
SO2		0.10	0.01	0.01	b.d.	b.d.	b.d.	b.d.	b.d.	b.d.
K2O		b.d.	b.d.	b.d.	b.d.	b.d.	b.d.	b.d.	b.d.	b.d.
La2O3		b.d.	b.d.	b.d.	b.d.	b.d.	b.d.	b.d.	b.d.	b.d.
Na2O		0.04	b.d.	b.d.	b.d.	b.d.	b.d.	b.d.	b.d.	b.d.
Al2O3		b.d.	b.d.	b.d.	b.d.	b.d.	b.d.	b.d.	b.d.	b.d.
SiO2		0.15	0.08	0.13	0.05	0.12	0.06	0.08	0.09	0.12
MgO		b.d.	b.d.	b.d.	b.d.	b.d.	b.d.	b.d.	b.d.	b.d.
F		2.46	2.50	2.46	2.42	2.39	2.45	2.21	2.58	2.42
Ce2O3		0.19	b.d.	0.18	0.07	0.12	b.d.	b.d.	b.d.	b.d.
O = (F,Cl)		1.13	1.13	1.11	1.09	1.07	1.11	1.00	0.00	1.10
OH wt% calc.		0.95	0.97	1.01	1.01	1.07	1.00	1.22	0.90	0.98
Total		100.66	101.08	100.58	99.66	100.43	99.90	100.43	101.78	98.79
S (µg/g)			56	46	b.d.	8	13	b.d.	12	7
Distance (µm)	0	10.61	21.23	31.84	42.46	53.07	63.68	74.3	84.91	95.52
F**		1.31	1.32	1.3	1.3	1.27	1.31	1.17	1.37	1.31
Cl**		0.12	0.1	0.09	0.09	0.09	0.09	0.09	0.09	0.1
OH**		0.57	0.58	0.61	0.61	0.64	0.6	0.73	0.54	0.59
F +Cl +OH		2	2	2	2	2	2	2	2	2

	Transect 3														
Sample	AA-Trans3-1	AA-Trans3-2	AA-Trans3-3	AA-Trans3-4	AA-Trans3-5	AA-Trans3-6	AA-Trans3-7	AA-Trans3-8	AA-Trans3-9	AA-Trans3-10	AA-Trans3-11	AA-Trans3-12	AA-Trans3-13	AA-Trans3-14	AA-Trans3-15
Cl	0.58	0.57	0.48	0.42	0.44	0.42	0.43	0.69	0.90	1.10	1.10	0.96	0.52	0.37	0.38
P2O5	41.52	41.17	41.12	41.25	41.43	40.44	41.16	40.90	40.56	41.03	41.19	41.66	40.65	41.78	41.87
CaO	54.16	54.74	55.03	54.82	54.77	54.87	55.07	54.78	53.52	53.72	54.52	54.36	55.03	55.09	55.06
MnO	b.d.	b.d.	b.d.	b.d.	b.d.	b.d.	b.d.	b.d.	b.d.	b.d.	b.d.	b.d.	b.d.	b.d.	b.d.
FeO	0.70	0.39	0.21	0.13	0.14	0.09	0.09	0.09	0.08	0.05	b.d.	b.d.	b.d.	b.d.	b.d.
TiO2	0.02	0.02	b.d.	b.d.	b.d.	b.d.	b.d.	b.d.	b.d.	b.d.	b.d.	b.d.	b.d.	b.d.	b.d.
SO2	0.16	0.08	b.d.	b.d.	0.01	0.01	b.d.	0.05	0.07	0.08	0.07	0.07	0.02	0.00	0.01
K2O	b.d.	b.d.	b.d.	b.d.	b.d.	b.d.	b.d.	b.d.	b.d.	b.d.	b.d.	b.d.	b.d.	b.d.	b.d.
La2O3	b.d.	b.d.	b.d.	b.d.	b.d.	b.d.	b.d.	b.d.	b.d.	b.d.	0.17	b.d.	b.d.	b.d.	b.d.
Na2O	0.11	0.08	b.d.	0.05	b.d.	b.d.	b.d.	0.05	0.10	0.15	0.13	0.09	0.06	b.d.	b.d.
Al2O3	b.d.	b.d.	b.d.	b.d.	b.d.	b.d.	b.d.	b.d.	b.d.	b.d.	b.d.	b.d.	b.d.	b.d.	b.d.
SiO2	0.12	0.11	0.11	0.12	0.12	0.19	0.13	0.12	0.11	0.12	0.11	0.12	0.07	0.11	0.13
MgO	b.d.	b.d.	b.d.	b.d.	b.d.	b.d.	b.d.	b.d.	b.d.	b.d.	b.d.	0.02	b.d.	b.d.	b.d.
F	2.25	2.54	2.55	2.51	2.40	2.38	2.38	2.37	2.19	2.14	2.05	2.34	2.41	2.53	2.44
Ce2O3	0.19	0.33	0.08	0.11	0.21	0.24	0.11	0.22	0.21	0.27	0.37	0.43	b.d.	0.17	b.d.
O = (F,Cl)	1.08	1.20	1.18	1.15	1.11	1.10	1.10	1.15	1.12	1.15	1.11	1.20	1.13	1.15	1.11
OH wt% calc.	1.04	0.78	0.8	0.87	0.96	0.95	0.98	0.85	0.88	0.85	0.94	0.77	0.88	0.9	0.98
Total	99.79	99.62	99.20	99.14	99.37	98.48	99.25	98.97	97.51	98.37	99.55	99.61	98.51	99.80	99.76
S (µg/g)			24	6	33	34	16	260	328	379	364	337	82	15	44
Distance (µm)	0	6.68	13.35	20.03	26.71	33.38	40.06	46.75	53.42	60.1	66.78	73.45	80.13	86.81	93.5
F**	1.21	1.37	1.38	1.36	1.29	1.3	1.28	1.28	1.2	1.17	1.11	1.26	1.31	1.35	1.3
Cl**	0.17	0.16	0.14	0.12	0.13	0.12	0.12	0.2	0.27	0.32	0.32	0.28	0.15	0.11	0.11
OH**	0.63	0.47	0.48	0.52	0.58	0.58	0.59	0.52	0.53	0.51	0.57	0.46	0.54	0.54	0.59
F +Cl +OH	2	2	2	2	2	2	2	2	2	2	2	2	2	2	2

	Transect 4									
Sample	Pyrrhotite	AA-Trans4-2	AA-Trans4-3	AA-Trans4-4	AA-Trans4-5	AA-Trans4-6	AA-Trans4-7	AA-Trans4-8	AA-Trans4-9	AA-Trans4-10*
Cl		0.39	0.41	0.43	0.42	0.45	0.51	0.57	0.29	
P2O5		41.23	41.35	41.46	41.04	41.68	41.91	40.65	35.23	
CaO		56.02	55.07	55.21	55.55	55.42	55.07	54.05	48.54	
MnO		b.d.	b.d.	b.d.	b.d.	b.d.	b.d.	b.d.	b.d.	
FeO		0.31	0.23	0.11	0.11	b.d.	0.19	0.28	1.93	
TiO2		b.d.	b.d.	b.d.	b.d.	b.d.	0.03	b.d.	b.d.	
SO2		0.03	0.01	0.01	0.00	b.d.	0.02	0.06	0.03	
K2O		b.d.	b.d.	b.d.	b.d.	b.d.	b.d.	b.d.	b.d.	
La2O3		b.d.	b.d.	b.d.	b.d.	b.d.	b.d.	b.d.	0.52	
Na2O		b.d.	b.d.	b.d.	b.d.	b.d.	b.d.	0.08	b.d.	
Al2O3		b.d.	b.d.	b.d.	b.d.	b.d.	b.d.	b.d.	b.d.	
SiO2		0.02	0.04	0.04	0.07	0.08	0.07	0.23	5.38	
MgO		b.d.	b.d.	b.d.	b.d.	b.d.	b.d.	b.d.	b.d.	
F		2.42	2.38	2.58	2.42	2.50	2.23	2.19	1.76	
Ce2O3		b.d.	b.d.	b.d.	b.d.	0.08	0.10	0.23	1.63	
O = (F,Cl)		1.10	1.09	1.18	1.11	1.15	1.05	1.05	0.81	
OH wt% calc.		0.98	0.99	0.81	0.95	0.89	1.10	1.06	1.55	
Total		100.29	99.39	99.46	99.45	99.94	100.17	98.35	96.07	
S (µg/g)		167	46	32	23	2	77	309	163	
Distance (µm)	0	8.33	16.66	24.99	33.32	41.65	49.98	58.31	66.64	
F**		1.29	1.28	1.39	1.3	1.34	1.19	1.19	0.97	
Cl**		0.11	0.12	0.12	0.12	0.13	0.15	0.17	0.09	
OH**		0.59	0.6	0.49	0.57	0.54	0.66	0.64	0.94	
F +Cl +OH		2	2	2	2	2	2	2	2	

	Transect 5								
Sample	Pyrrhotite	AA-Trans5-2	AA-Trans5-3	AA-Trans5-4	AA-Trans5-5	AA-Trans5-6	AA-Trans5-7	SD wt% oxide	Det limit (µg/g):
Cl		0.40	0.44	0.51	0.43	0.40	0.49	0.06	226
P2O5		41.70	41.62	42.37	41.93	41.74	41.62	1.22	1197
CaO		55.59	55.03	54.92	55.65	55.43	54.59	0.72	387
MnO		b.d.	b.d.	b.d.	b.d.	b.d.	b.d.	0.06	522
FeO		0.32	0.12	0.12	0.07	0.06	0.09	0.14	540
TiO2		b.d.	b.d.	b.d.	b.d.	b.d.	b.d.	0.04	311
SO2		0.03	0.01	0.07	b.d.	0.01	0.06	0.07	58
K2O		b.d.	b.d.	b.d.	b.d.	b.d.	b.d.	0.03	317
La2O3		b.d.	b.d.	b.d.	b.d.	b.d.	b.d.	0.11	1057
Na2O		b.d.	b.d.	0.06	b.d.	b.d.	0.14	0.04	367
Al2O3		b.d.	b.d.	b.d.	b.d.	b.d.	b.d.	0.04	219
SiO2		0.05	0.05	0.06	0.05	0.04	0.10	0.06	253
MgO		0.02	b.d.	b.d.	b.d.	b.d.	b.d.	0.04	256
F		2.41	2.54	2.41	2.40	2.29	2.41	0.35	2837
Ce2O3		b.d.	b.d.	0.23	b.d.	b.d.	0.27	0.10	1224
O = (F,Cl)		1.11	1.17	1.13	1.11	1.05	1.13		
OH wt% calc.		0.99	0.85	0.95	0.99	1.09	0.93		
Total		100.43	99.50	100.57	100.41	100.00	99.57		
S (µg/g)		155	30	332	5	57	316		
Distance (µm)	0	15.28	30.57	45.85	61.14	76.42	91.71		
F**		1.29	1.36	1.28	1.28	1.22	1.3		
Cl**		0.11	0.13	0.14	0.12	0.11	0.14		
OH**		0.6	0.51	0.57	0.6	0.66	0.56		
F +Cl +OH		2	2	2	2	2	2		

Notes:

SD wt% oxide and det limit are averages

Calculated as OH assuming the halogen site is filled with F + Cl + OH. O=F,Cl is correction factor

n=38

b.d. is bellow detection limit

SD wt% averages are presented for each oxide. SD for F and Cl represented in Wt%.

*Mixed analysis

**Anion Ratio for Ternary Plot

Supplementary Data Table S5. XANES Standards
APS Standards

Energy	Na2SO3 - APS 13-ID-E standard database APS
2460	0.000881035
2462	0.000796707
2464	-0.00247132
2464.15	-0.000171231
2464.301	-0.001279924
2464.45	-7.82448E-05
2464.601	-0.001149123
2464.75	-0.000396334
2464.899	0.000401589
2465.05	0.000111387
2465.2	0.000519553
2465.35	-0.000387234
2465.5	0.000468602
2465.65	-0.000384513
2465.8	0.00144473
2465.95	0.001694321
2466.1	-0.000307854
2466.25	0.000429661
2466.4	0.002700474
2466.551	0.001527131
2466.7	0.002109148
2466.851	0.001392013
2467	0.002625407
2467.15	0.002937209
2467.3	0.004335859
2467.45	0.005650342
2467.6	0.005949946
2467.75	0.006098293
2467.9	0.008010482
2468.05	0.007218357
2468.2	0.009314738
2468.351	0.009997943
2468.5	0.00962363
2468.65	0.012839794
2468.801	0.013182673
2468.951	0.015148534
2469.101	0.018922151
2469.25	0.01796233
2469.401	0.021171758
2469.551	0.025060036
2469.7	0.031292204
2469.85	0.040225608
2470	0.048969943
2470.15	0.058809664
2470.301	0.067647287
2470.45	0.079286863
2470.601	0.093350143
2470.75	0.10135591
2470.9	0.10816685
2471.05	0.11920564
2471.2	0.13300486
2471.351	0.15341602
2471.5	0.18084357
2471.65	0.21151396
2471.8	0.24899209
2471.95	0.27942461
2472.1	0.29999254
2472.25	0.30570566
2472.4	0.30363395
2472.55	0.30078767
2472.7	0.2984037
2472.85	0.30015487
2472.999	0.3051282
2473.15	0.3043086
2473.3	0.31496071
2473.449	0.32380937
2473.601	0.3346566
2473.75	0.35190851
2473.901	0.37031797
2474.051	0.38642872
2474.2	0.39942716
2474.351	0.40269514
2474.5	0.40059724
2474.649	0.39816633
2474.8	0.39666364
2474.95	0.39188152
2475.101	0.40106557
2475.251	0.40367305
2475.4	0.41511502
2475.55	0.44220282
2475.7	0.46903569
2475.85	0.50646869
2476	0.55286484
2476.15	0.61474523
2476.301	0.68600775
2476.45	0.78543691
2476.6	0.90434089
2476.75	1.0670177
2476.9	1.2814607
2477.05	1.5308902
2477.2	1.9344169
2477.351	2.0340412
2477.5	2.214873
2477.65	2.302173
2477.8	2.3447792
2477.95	2.3320463
2478.1	2.2778132
2478.25	2.1788058
2478.401	2.0329547
2478.55	1.8596897
2478.7	1.6322657
2478.85	1.4340148
2479	1.2794683
2479.15	1.1724845
2479.3	1.1055678
2479.45	1.0736621
2479.6	1.0516062
2479.75	1.0514448
2479.9	1.0682715
2480.05	1.0951105
2480.2	1.1345903
2480.35	1.2073136
2480.5	1.2797588
2480.65	1.3948313
2480.8	1.4892086
2480.949	1.5909969
2481.1	1.6929534
2481.25	1.7764391
2481.4	1.8676132
2481.55	1.9438336
2481.7	2.0172729
2481.85	2.0828005
2482	2.1042577
2482.15	2.0912614
2482.3	2.069147
2482.45	2.0159666
2482.6	1.9471592
2482.75	1.859962
2482.9	1.7681917
2483.05	1.6747734
2483.2	1.6004073
2483.351	1.5303795
2483.5	1.471369
2483.65	1.4284874
2483.8	1.3842055
2483.951	1.352371
2484.101	1.320264
2484.25	1.2959302
2484.4	1.281891
2484.551	1.2614654
2484.7	1.2516449
2484.85	1.23652
2485	1.2163256
2485.15	1.1942271
2485.301	1.1848994
2485.45	1.1644677
2485.6	1.1423644
2485.75	1.1364869
2485.901	1.1158564
2486.05	1.1024838
2486.2	1.0915453
2486.35	1.0891235
2486.5	1.0933911
2486.65	1.0862438
2486.8	1.0950369
2486.95	1.1045083
2487.1	1.1095834
2487.25	1.1226495
2487.401	1.1399002
2487.55	1.1414324
2487.7	1.1591667
2487.851	1.1616577
2488	1.1643073
2488.79	1.1781706
2489.598	1.1998134
2490.426	1.2204907
2491.273	1.2014061
2492.139	1.1844647
2493.023	1.1885414
2493.927	1.2195582
2494.851	1.2660831
2495.792	1.2969165
2496.753	1.3400035
2497.733	1.346
2498.731	1.3232829
2499.75	1.277115
2500.786	1.2140712
2501.843	1.157307
2502.917	1.1202428
2504.011	1.0900481
2505.125	1.0572936
2506.257	1.0219649
2507.408	0.99783282
2508.578	0.99004386
2509.766	0.98095286
2510.975	0.98044691
2512.202	0.97171773
2513.448	0.95808867
2514.714	0.95893818
2515.998	0.94850642
2517.302	0.94777767
2518.624	0.94195329
2519.964	0.93821673
2521.325	0.93645507
2522.704	0.93777903
2524.103	0.93903656
2525.52	0.94607305
2526.957	0.96089991
2528.412	0.96323788
2529.886	0.96373524
2531.38	0.97487731
2532.892	0.97955025
2534.424	0.98460566
2535.975	0.99278386
2537.545	0.99455084
2539.133	0.9877433
2540.74	0.98399511

Energy	S2- Pyrrhotite
2460	0.00933404
2461	0.01211981
2462	0.015686407
2463	0.021299255
2464	0.028261233
2464.2	0.030327636
2464.4	0.032676443
2464.6	0.034636312
2464.8	0.037087191
2465	0.040287117
2465.2	0.043666539
2465.4	0.046898013
2465.6	0.051209843
2465.8	0.055552445
2466	0.06131938
2466.2	0.066690863
2466.4	0.074453595
2466.6	0.082181631
2466.8	0.090212642
2467	0.10382453
2467.2	0.1189469
2467.4	0.13893671
2467.6	0.16596727
2467.8	0.19683883
2468	0.25547491
2468.2	0.33522958
2468.4	0.46214015
2468.6	0.65023318
2468.8	0.86323412
2469	1.0323196
2469.2	1.1539864
2469.4	1.1793685
2469.6	1.1671784
2469.8	1.157021
2470	1.1492461
2470.2	1.1409487
2470.4	1.1094941
2470.6	1.0544862
2470.8	0.98599399
2471	0.91052999
2471.2	0.84059537
2471.4	0.78160235
2471.6	0.73032791
2471.8	0.69810226
2472	0.67821005
2472.2	0.67333687
2472.4	0.68239763
2472.6	0.71128675
2472.8	0.7432044
2473	0.80023652
2473.2	0.85511089
2473.4	0.90494552
2473.6	0.95160261
2473.8	0.99220187
2474	1.0283377
2474.2	1.058106
2474.4	1.0844621
2474.6	1.1066895
2474.8	1.1242308
2475	1.1366776
2475.2	1.1512229
2475.4	1.1633705
2475.6	1.1718456
2475.8	1.1814488
2476	1.1939353
2476.2	1.1918994
2476.4	1.2043173
2476.6	1.2145732
2476.8	1.2140896
2477	1.2197936
2477.2	1.2201376
2477.4	1.2218377
2477.6	1.2169107
2477.8	1.2222807
2478	1.2369595
2478.2	1.2131692
2478.4	1.2135097
2478.6	1.2125713
2478.8	1.2084179
2479	1.2021576
2479.2	1.1926392
2479.4	1.1810442
2479.6	1.1669445
2479.8	1.1461621
2480	1.1283347
2480.2	1.1031495
2480.4	1.0844153
2480.6	1.0652984
2480.8	1.0472154
2481	1.022786
2481.2	1.0062882
2481.4	0.98927988
2481.6	0.98306063
2481.8	0.98196513
2482	0.9826861
2482.2	0.99103268
2482.4	0.99666277
2482.6	1.0038673
2482.8	1.0116953
2483	1.0168409
2483.2	1.0200727
2483.4	1.0268908
2483.6	1.0263721
2483.8	1.0214204
2484	1.0239918
2484.2	1.0246544
2484.4	1.0220025
2484.6	1.0190828
2484.8	1.0212074
2485	1.0219927
2485.2	1.022359
2485.4	1.0236472
2485.6	1.0179907
2485.8	1.0147895
2486	1.0115598
2486.2	1.0130459
2486.4	1.0085605
2486.6	1.006214
2486.8	1.0023615
2487	1.0026271
2487.2	1.0027826
2487.4	1.0010935
2487.6	0.99332836
2487.8	0.99218437
2488	0.99179272
2489	0.98662426
2490	0.98217868
2491	0.97730614
2492	0.97083355
2493	0.96287007
2494	0.96571296
2495	0.96974841
2496	0.9752978
2497	0.97633385
2498	0.98078894
2499	0.98673317
2500	0.99803393
2501	1.0021854
2502	1.0151937
2503	1.0311509
2504	1.0426524
2505	1.0516389
2508	1.0537671
2509	1.0544208
2510	1.0451712
2511	1.0431967
2512	1.0446611
2513	1.0464388
2514	1.0322455
2515	1.0149208
2516	0.99773217
2517	0.98620353
2518	0.97131783
2519	0.95918431
2520	0.95181401
2521	0.94824553
2522	0.93738387
2523	0.93068597
2524	0.92516965
2525	0.91970937
2526	0.93736858
2527	0.94718669
2528	0.9515959
2529	0.95876133
2530	0.96643524
2531	0.97190685
2532	0.98175227
2533	0.98857769
2534	0.99283571
2536	0.99495495
2537	0.99746424
2538	1.0035692
2539	1.0088169
2540	1.0100599
	1.0064098
	1.0057766
	1.0056433

Energy	S1- Pyrite
2460	0.008489022
2461	0.002738127
2462	-0.000555497
2463	-0.005287535
2464	-0.005791297
2464.2	-0.006017737
2464.4	-0.005402453
2464.6	-0.003439574
2464.8	-0.001878018
2465	-0.00357904
2465.2	-0.004304387
2465.4	-0.000251441
2465.6	0.001043916
2465.8	0.004573896
2466	0.006803863
2466.2	0.012858155
2466.4	0.017053003
2466.6	0.018853136
2466.8	0.025115012
2467	0.02860363
2467.2	0.034984126
2467.4	0.045829967
2467.6	0.052524123
2467.8	0.063984843
2468	0.077937604
2468.2	0.093253935
2468.4	0.10679044
2468.6	0.13120001
2468.8	0.15791143
2469	0.19326056
2469.2	0.22491524
2469.4	0.29579863
2469.6	0.35417104
2469.8	0.48071935
2470	0.626593
2470.2	0.83265418
2470.4	1.1171703
2470.6	1.399413
2470.8	1.6142305
2471	1.7433312
2471.2	1.7992524
2471.4	1.8083236
2471.6	1.7720336
2471.8	1.7262335
2472	1.6808401
2472.2	1.6162681
2472.4	1.5541102
2472.6	1.4705414
2472.8	1.3764291
2473	1.280385
2473.2	1.1957071
2473.4	1.0952554
2473.6	1.0004905
2473.8	0.89464703
2474	0.80803431
2474.2	0.73856868
2474.4	0.68415837
2474.6	0.63609985
2474.8	0.61518569
2475	0.58527434
2475.2	0.56608584
2475.4	0.56481756
2475.6	0.57524374
2475.8	0.60358057
2476	0.65600718
2476.2	0.7465651
2476.4	0.81016178
2476.6	0.95346457
2476.8	1.0033488
2477	1.0299767
2477.2	1.0482642
2477.4	1.074149
2477.6	1.0675263
2477.8	1.0951462
2478	1.1077388
2478.2	1.128244
2478.4	1.1473094
2478.6	1.1508075
2478.8	1.15876
2479	1.1749774
2479.2	1.1683358
2479.4	1.1689228
2479.6	1.1677965
2479.8	1.1678431
2480	1.1732004
2480.2	1.1514468
2480.4	1.1285875
2480.6	1.1126498
2480.8	1.1114787
2481	1.0920017
2481.2	1.0959709
2481.4	1.087052
2481.6	1.0829131
2481.8	1.0731428
2482	1.0752867
2482.2	1.0653097
2482.4	1.0815741
2482.6	1.0907573
2482.8	1.0920449
2483	1.1108329
2483.2	1.1207064
2483.4	1.1215582
2483.6	1.1304109
2483.8	1.1394704
2484	1.1338848
2484.2	1.1296673
2484.4	1.1338358
2484.6	1.1361886
2484.8	1.1448482
2485	1.154594
2485.2	1.1577303
2485.4	1.1693426
2485.6	1.1727393
2485.8	1.1707985
2486	1.1714232
2486.2	1.1711324
2486.4	1.1685553
2486.6	1.1638344
2486.8	1.1472173
2487	1.1529104
2487.2	1.1574976
2487.4	1.1603501
2487.6	1.1554838
2487.8	1.1518933
2488	1.1521956
2489	1.1655162
2490	1.174905
2491	1.1665923
2492	1.174994
2493	1.1558694
2494	1.1161783
2495	1.0948926
2496	1.0650898
2497	1.042372
2498	1.0177015
2499	0.98317937
2500	0.95140752
2501	0.93144153
2502	0.9235019
2503	0.93697348
2504	0.9486459
2505	0.9646054
2506	0.97275302
2507	0.98036537
2508	0.98755223
2509	0.98648391
2510	1.0013873
2511	1.0132592
2512	1.0234947
2513	1.0409557
2514	1.0561767
2515	1.0699114
2516	1.0805613
2517	1.0891811
2518	1.0875393
2519	1.0731493
2520	1.0610586
2521	1.0507196
2522	1.038488
2523	1.0241449
2524	1.0189896
2525	1.0057139
2526	0.98915971
2527	0.97704044
2528	0.97172566
2529	0.96414543
2530	0.96286506
2531	0.96390894
2532	0.95848974
2533	0.96006615
2534	0.96327071
2535	0.96445797
2536	0.97247301
2537	0.98450265
2538	0.99072034
2539	1.0023323
2540	1.0131283
2541	
2542	
2543	
2544	
2545	
2546	
2547	
2548	
2549	
2550	
2551	
2552	
2553	
2554	
2555	
2556	
2557	
2558	
2559	
2560	

Energy	Durango Apatite
2460	0.0049
2462	0.0095
2464	-0.0018
2464.3	-0.0052
2464.6	-0.0113
2464.9	-0.0166
2465.2	-0.012
2465.5	0.0107
2465.8	0.0123
2466.1	0.0097
2466.4	-0.017
2466.7	-0.0053
2467	-0.0086
2467.3	-0.0164
2467.6	-0.0249
2467.9	-0.004
2468.2	0.022
2468.5	0.0122
2468.8	-0.0109
2469.1	0.0273
2469.4	0.0479
2469.7	0.0531
2470	0.0811
2470.3	0.0905
2470.6	0.1112
2470.9	0.1081
2471.2	0.1314
2471.5	0.1615
2471.8	0.1409
2472.1	0.119
2472.4	0.1213
2472.7	0.1167
2473	0.1437
2473.3	0.1518
2473.6	0.1772
2473.9	0.1511
2474.2	0.1834
2474.5	0.2103
2474.8	0.2066
2475.1	0.2211
2475.4	0.2492
2475.7	0.3065
2476	0.3248
2476.3	0.3807
2476.6	0.4637
2476.9	0.6666
2477.2	0.9384
2477.5	1.077
2477.8	1.0033
2478.1	0.8046
2478.4	0.6202
2478.7	0.5555
2479	0.6364
2479.3	0.6634
2479.6	0.8159
2479.9	1.1414
2480.2	1.6773
2480.5	2.6448
2480.8	4.3871
2481.1	6.6871
2481.4	8.7387
2481.7	9.7379
2482	9.398
2482.3	7.7701
2482.6	5.3229
2482.9	3.2384
2483.2	2.0985
2483.5	1.5771
2483.8	1.3277
2484.1	1.2599
2484.4	1.2636
2484.7	1.3112
2485	1.3687
2485.3	1.3828
2485.6	1.3384
2485.9	1.2641
2486.2	1.1692
2486.5	1.0749
2486.8	1.0014
2487.1	0.8814
2487.4	0.8562
2487.7	0.8143
2488	0.8441
2490	1.0665
2492	1.4788
2494	1.5717
2496	1.6217
2498	1.7884
2500	1.7771
2502	1.4721
2504	1.2367
2506	1.1759
2508	1.1003
2510	1.0296
2512	0.9549
2514	0.9266
2516	0.9834
2518	1.0099
2520	1.0112
2522	0.9978
2524	1.0103
2526	1.0359
2528	1.0596
2530	1.0274
2532	1.0099
2534	0.991
2536	0.9522
2538	0.9455
2540	0.9209

Energy	Clear double sided adhesive tape
2459.5	-0.0021
2462	0.0043
2464.5	-0.0021
2467	0.0116
2467.1	0.0195
2467.2	0.0186
2467.3	0.0198
2467.4	0.0275
2467.5	0.0285
2467.6	0.0354
2467.7	0.025
2467.8	0.0253
2467.9	0.031
2468	0.0387
2468.1	0.0411
2468.2	0.0548
2468.3	0.0575
2468.4	0.071
2468.5	0.0803
2468.6	0.1038
2468.7	0.1192
2468.8	0.1343
2468.9	0.1659
2469	0.1659
2469.1	0.1621
2469.2	0.1548
2469.3	0.149
2469.4	0.1343
2469.5	0.115
2469.6	0.112
2469.7	0.1001
2469.8	0.0994
2469.9	0.1011
2470	0.1077
2470.1	0.1057
2470.2	0.1139
2470.3	0.1169
2470.4	0.1314
2470.5	0.1425
2470.6	0.1526
2470.7	0.1756
2470.8	0.2171
2470.9	0.2488
2471	0.279
2471.1	0.3274
2471.2	0.3918
2471.3	0.45
2471.4	0.5264
2471.5	0.6384
2471.6	0.7298
2471.7	0.847
2471.8	0.9536
2471.9	1.0912
2472	1.2103
2472.1	1.3211
2472.2	1.4029
2472.3	1.5156
2472.4	1.542
2472.5	1.6478
2472.6	1.6717
2472.7	1.6886
2472.8	1.6969
2472.9	1.673
2473	1.6482
2473.1	1.6298
2473.2	1.5924
2473.3	1.5616
2473.4	1.5097
2473.5	1.4402
2473.6	1.3762
2473.7	1.332
2473.8	1.286
2473.9	1.2271
2474	1.1918
2474.1	1.1278
2474.2	1.112
2474.3	1.088
2474.4	1.0575
2474.5	1.0571
2474.6	1.0265
2474.7	1.0211
2474.8	1.0136
2474.9	0.9996
2475	0.9885
2475.1	0.9854
2475.2	0.974
2475.3	0.9807
2475.4	0.9698
2475.5	0.958
2475.6	0.941
2475.7	0.9438
2475.8	0.9431
2475.9	0.9472
2476	0.9683
2476.1	0.9517
2476.2	0.9501
2476.3	0.9444
2476.4	0.9503
2476.5	0.958
2476.6	0.9792
2476.7	1.0448
2476.8	0.9679
2476.9	0.9762
2477	1.0022
2477.1	1.0101
2477.2	0.9992
2477.3	1.0325
2477.4	1.0398
2477.5	1.0722
2477.6	1.054
2477.7	1.0339
2477.8	1.0481
2477.9	1.0588
2478	1.0664
2478.1	1.0689
2478.2	1.0717
2478.3	1.1066
2478.4	1.1102
2478.5	1.1056
2478.6	1.1314
2478.7	1.1431
2478.8	1.1616
2478.9	1.1851
2479	1.2115
2479.1	1.2345
2479.2	1.2893
2479.3	1.3367
2479.4	1.3627
2479.5	1.4214
2479.6	1.4511
2479.7	1.518
2479.8	1.5735
2479.9	1.6058
2480	1.6287
2480.1	1.6282
2480.2	1.6372
2480.3	1.6559
2480.4	1.6985
2480.5	1.6915
2480.6	1.7668
2480.7	1.7588
2480.8	1.8175
2480.9	1.8626
2481	1.9531
2481.1	2.0093
2481.2	2.0824
2481.3	2.1544
2481.4	2.2051
2481.5	2.3934
2481.6	2.4841
2481.7	2.5219
2481.8	2.5478
2481.9	2.5504
2482	2.538
2482.1	2.4969
2482.2	2.3968
2482.3	2.3232
2482.4	2.2142
2482.5	2.1247
2482.6	2.0104
2482.7	1.8858
2482.8	1.7857
2482.9	1.7223
2483	1.6252
2483.1	1.555
2483.2	1.4819
2483.3	1.431
2483.4	1.3741
2483.5	1.3278
2483.6	1.2967
2483.7	1.2649
2483.8	1.246
2483.9	1.2333
2484	1.232
2484.1	1.2147
2484.2	1.2003
2484.3	1.1809
2484.4	1.1737
2484.5	1.1756
2484.6	1.1689
2484.7	1.151
2484.8	1.1516
2484.9	1.1582
2485	1.1492
2485.1	1.1455
2485.2	1.1514
2485.3	1.1521
2485.4	1.1638
2485.5	1.1376
2485.6	1.1564
2485.7	1.1444
2485.8	1.14
2485.9	1.1475
2486	1.156
2486.1	1.147
2486.2	1.146
2486.3	1.1435
2486.4	1.1401
2486.5	1.1469
2486.6	1.1452
2486.7	1.1323
2486.8	1.1346
2486.9	1.1262
2487	1.1214
2489.0109	1.0967
2491.0217	1.0885
2493.0326	1.101
2495.0435	1.1285
2497.0543	1.1716
2499.0652	1.1447
2501.0761	1.1034
2503.087	1.0524
2505.0978	1.0068
2507.1087	0.9828
2509.1196	0.9786
2511.1304	0.9947
2513.1413	1.0102
2515.1522	1.0032
2517.163	1.0115
2519.1739	1.0197
2521.1848	1.0006
2523.1957	0.9899
2525.2065	1.0073
2527.2174	1.0027
2529.2283	0.9815
2531.2391	1.0028
2533.25	0.9999
2535.2609	0.9919
2537.2717	0.9948
2539.2826	0.9823